Transportation Research Part C 83 (2017) 39–60

Contents lists available at ScienceDirect

Transportation Research Part C

journal homepage: www.elsevier.com/locate/trc

Scalable stability analysis on large connected vehicle systems subject to stochastic communication delays

Wubing B. Qin *, Gábor Orosz

Department of Mechanical Engineering, University of Michigan, Ann Arbor, MI 48109, USA

ARTICLE INFO

Article history:
Received 9 March 2017
Received in revised form 10 July 2017
Accepted 11 July 2017

Keywords:
DSRC
V2V
Stochastic delays
Open chain
Closed ring
Plant stability
String stability
Mean dynamics
Covariance dynamics
Second moment dynamics

ABSTRACT

In this paper large connected vehicle systems are analyzed where vehicles utilize vehicle-to-vehicle (V2V) communication to control their longitudinal motion. It is shown that packet drops in communication channels introduce stochastic delay variations in the feedback loops. Scalable methods are developed to evaluate stability and disturbance attenuation while utilizing the mean, second moment, and covariance dynamics in open chain and closed ring configurations. The stability results are summarized using stability diagrams in the plane of the control parameters while varying the packet delivery ratio and the number of vehicles. Also, the relationship between the stability of different configurations is characterized. The results emphasize the feasibility of V2V communication-based control in improving traffic flow.

Published by Elsevier Ltd.

1. Introduction

The past decades witnessed a worldwide increase in the number of vehicles on the road, bringing major concerns about traffic congestions (Schrank et al., 2015). The large reaction time and limited perception range of human drivers make them unable to maintain smooth traffic flow and may trigger stop-and-go traffic jams while reacting to unexpected events (Orosz et al., 2009, 2010). On the other hand, advanced driver assistant systems (ADAS) can be used to improve the longitudinal control of vehicles. Although such technologies typically target at the enhancement of safety and driving comfort, they have an enormous potential in improving the efficiency of large scale traffic systems.

For example, adaptive cruise control (ACC) can be used to maintain a velocity-dependent inter-vehicle distance based on range sensors (radar or lidar) (Shladover, 1991; Ioannou and Chien, 1993; Rajamani and Zhu, 2002). It was demonstrated in (Werf et al., 2002; Davis, 2007) that due to faster and more accurate sensing abilities ACC may have a positive impact on traffic flow when the penetration rate of ACC vehicles is high enough. However, due to the high cost of range sensors and the perception limitation within the line of sight, this technology is still not widely available. To overcome the limitations, it was proposed to augment ACC with wireless V2V communication. This can allow vehicles to monitor the kinematic properties of other vehicles, even those beyond the line of sight, and they may utilize such information in their controllers to improve their safety and fuel economy and to mitigate traffic jams. In the US dedicated short range communication (DSRC)

* Corresponding author.
E-mail addresses: wubing@umich.edu (W.B. Qin), orosz@umich.edu (G. Orosz).

http://dx.doi.org/10.1016/j.trc.2017.07.005
0968-090X/Published by Elsevier Ltd.

has been standardized (Kenney, 2011; SAE J2735, 2016) for V2V communication to foster this idea. An overview of vehicular control with V2V communication can be found in (Li et al., 2015).

One strategy is called cooperative adaptive cruise control (CACC) (Naus et al., 2010; Desjardins and Chaib-draa, 2011; Milanes et al., 2014; Jia and Ngoduy, 2016) that assigns a fixed communication topology to a group of ACC vehicles: each vehicle monitors the motion of the preceding vehicle using range sensors, as well as the motion of the group leader via V2V communication. This technology was shown to be able to improve traffic throughput with a high enough penetration rate using simulations (van Arem et al., 2006; Milanes et al., 2011; Ploeg et al., 2014b, 2015; di Bernardo et al., 2015; Zheng et al., 2016b; Talebpour and Mahmassani, 2016; Lioris et al., 2017) and fruitful experiments have been conducted in the PATH program (Rajamani and Shladover, 2001), the SARTRE project (Chan et al., 2012), and grand cooperative driving challenge (Ploeg et al., 2012). However, the harsh requirement that all the vehicles must be equipped with range sensors, DSRC devices and controllers hinders the deployment of such strategy.

Alternatively, another control strategy, referred to as connected cruise control (CCC), has been proposed that does not require every vehicle to be equipped with range sensors and DSRC devices. A CCC vehicle utilizes all the available V2V information from vehicles ahead within the communication range (Ge and Orosz, 2014; Zhang and Orosz, 2016; Orosz, 2016). Such flexibility allows controllers to fully exploit the advantages of V2V communication while gathering information from vehicles within and beyond the line of sight. This includes scenarios when the vehicle immediately ahead is hidden by the road geometry and cannot be detected by range sensors (such as radar or lidar). Different aspects of CCC have been studied, such as the influence of communication delays, connectivity topology, nonlinearities and optimal design (Avedisov and Orosz, 2015; Zhang and Orosz, 2017; Ge and Orosz, 2017; Ge et al., 2017), and it was demonstrated that this strategy has a large potential in improving traffic flow.

In Qin et al. (2017), the two major aspects of V2V communication-based control of connected vehicle systems were considered for the simplest CCC system – a predecessor-follower pair; see Fig. 1(a). To incorporate intermittency in communication requires consideration of time delays and digital effects (Qin and Orosz, 2013), while to understand the effects of packet drops requires the characterization of the dynamics in the presence of stochastic delays. The mathematical tools created in (Qin et al., 2017) enabled us to analyze stochastic stability and stochastic disturbance attenuation (often referred to as string stability) in the vicinity of the equilibrium in simple connected vehicle systems. In particular, the concept of $n\sigma$ string stability was established that guarantees the attenuation of velocity fluctuations for trajectories that are within the n times standard deviation about the mean. A natural question to ask is whether such stability results are scalable for large stochastic connected vehicle systems; see (Zheng et al., 2016a) for scalability of stability for deterministic cases.

In this paper, we extend the notion of *$n\sigma$ string stability* to an open chain containing arbitrarily large numbers of connected vehicles (while still keeping the simplification that each vehicle only reacts to the motion of the vehicle immediately ahead). To ensure scalability, a set of decomposition methods is developed to significantly reduce the size of matrices appearing in the mean, second moment, and covariance dynamics. Moreover, the notion of *$n\sigma$ offset string stability* is proposed to characterize stability and disturbance attenuation as the number of vehicles is increased. This way the feasible ranges of control parameters that ensure smooth traffic flow can be characterized analytically as the number of vehicles increases towards infinity. Then, we also study the behavior of a system of arbitrary number of connected vehicles on a ring road. Similar to the open chain system, decomposition methods are developed to make the stability analysis scalable. The stability diagrams obtained unveil the relationships between large systems of connected vehicles of different configurations. Clearly, such comparison is not possible using numerical simulations considering the large system size and the requirement for enormous realizations given by the stochastically varying delays.

This paper is organized as follows. In Section 2, we provide the dynamics of a vehicle model and design a controller based on the information received via wireless communication subject to stochastic packet drops. In Sections 3 and 4, an open chain and a closed ring of connected vehicles are studied and the results are summarized using stability diagrams. In Section 5, the results of the open chain and the closed ring systems are compared to each other. Finally, we arrive at some conclusions in Section 6.

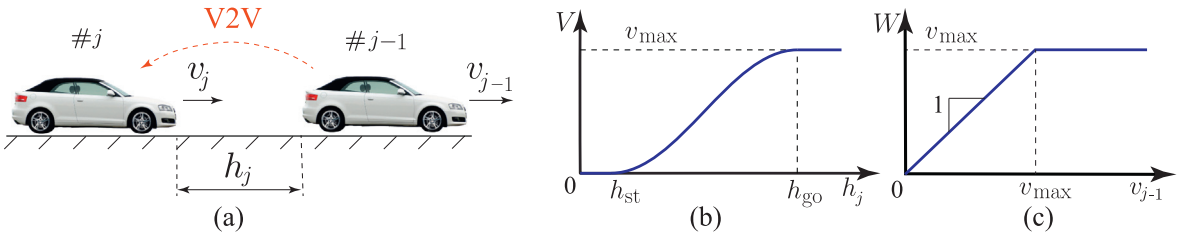

Fig. 1. (a) Predecessor-follower pair equipped with V2V communication on a single lane. Dashed red arrow indicates the information flow through wireless communication. (b) Range policy function (6). (c) Saturation function (7).

2. Feedback control with stochastic delays

We first start with describing the predecessor-follower pair shown in Fig. 1(a), where the control output of the j-th vehicle is based on the information received from the $(j-1)$-th vehicle. Similar to the setup in (Qin et al., 2017), we make the following assumptions: (i) The inter-vehicle distance h_j (called distance headway), can be calculated from GPS coordinates of the vehicles with adequate accuracy. (ii) each vehicle broadcasts its kinematic information intermittently with the sampling time Δt via DSRC devices subject to stochastic packet drops. (iii) A nonlinear controller with zero-order-hold, that acts on the distance headway h_j, the predecessor's velocity v_{j-1}, and the vehicle's ego velocity v_j, is implemented. (iv) The clocks of the predecessor and follower are synchronized and aligned.

For simplicity, we consider zero inclination and omit rolling resistance and air drag effects in the physics-based model (Orosz, 2016). This leads to the simplified vehicle dynamics

$$\begin{aligned} \dot{h}_j(t) &= v_{j-1}(t) - v_j(t), \\ \dot{v}_j(t) &= u_j(t_{k-\tau_j(k)}), \end{aligned} \tag{1}$$

for $t_k \leq t < t_{k+1}$, where $u_j(t)$ is the controller and the delay $\tau_j(k)$ is a stochastic variable due to stochastic packet drops. We assume that the controller outputs a command based on the newest information received via V2V communication from the vehicle ahead.

We remark that the framework presented in this paper allows vehicle models of different levels of fidelity. In particular, it was shown in (Orosz, 2016) that the stability results remain similar when realistic vehicle dynamics is incorporated (Zheng et al., 2016a). One may also incorporate the engine dynamics (Zheng et al., 2016a) as well but that may influence the stability results. Here we omit these effects and use the simple model (1) to gain insights to the effects of digital control with stochastic packet drops. The analysis of higher fidelity vehicle models is left for future research.

With the assumption that each packet delivery is a Bernoulli trial with the successful packet delivery ratio denoted as p, the stochastic variable $\tau_j(k)$ can be interpreted as number of trials to achieve one successful packet delivery. Thus, the probability distributions of the stochastic variable $\tau_j(k)$-s are identically geometrically distributed for each discrete time instant k with distribution

$$f_{\tau_j(k)}(\xi) = \sum_{r=1}^{\infty} w_r \delta(\xi - r), \tag{2}$$

where $\delta(\cdot)$ denotes the Dirac delta function and the weights are given by

$$w_r = p(1-p)^{r-1}, \qquad r = 1, \ldots, \infty. \tag{3}$$

One may notice that the distribution (3) has infinite many supports but the probabilities are rather small for large r values. Thus, we truncate the distribution (3) with the assumption that the maximum value of $\tau_j(k)$ is N, such that $\sum_{r=1}^{N-1} w_r \geqslant p_{\rm cr}$ and $p_{\rm cr}$ is the critical cumulative packet delivery ratio. This yields the truncated probability density function (PDF)

$$w_r = \begin{cases} p(1-p)^{r-1} & \text{if } r = 1, \ldots, N-1, \\ 1 - \sum_{i=1}^{N-1} w_i = (1-p)^{N-1} & \text{if } r = N, \\ 0 & \text{if } r > N. \end{cases} \tag{4}$$

Moreover, throughout this paper, we will assume that $\tau_j(k)$-s are independently, identically distributed (IID) with the distribution (2) and (4). More complicated (non-IID) stochastic processes were considered in (Qin et al., 2017).

We choose the nonlinear controller

$$u_j(t) = K_{\rm p}\big(V(h_j(t)) - v_j(t)\big) + K_{\rm v}\big(W(v_{j-1}(t)) - v_j(t)\big), \tag{5}$$

to regulate the inter-vehicle distance and velocity. The linearized version of this controller is also widely used in the literature (Naus et al., 2010; Lidström et al., 2012; Nieuwenhuijze et al., 2012; Ploeg et al., 2014a; Wang et al., 2014).

The range policy $V(h_j)$ gives the desired velocity as a function of distance headway h_j, and must be

- continuous and monotonously increasing (the more sparse the traffic is, the faster the vehicles intend to run);
- zero for $h_j \leq h_{\rm st}$ (vehicles intend to stop within a safety distance);
- maximal for $h_j \geq h_{\rm go}$ (vehicles intend to run with a given maximum speed in sparse traffic – often referred to as free flow).

Here we select the continuously differentiable range policy

$$V(h_j) = \begin{cases} 0 & \text{if} \quad h_j \leqslant h_{\rm st}, \\ \frac{v_{\max}}{2}\left(1 - \cos\left(\pi \frac{h_j - h_{\rm st}}{h_{\rm go} - h_{\rm st}}\right)\right) & \text{if} \quad h_{\rm st} < h_j < h_{\rm go}, \\ v_{\max} & \text{if} \quad h_j \geqslant h_{\rm go}, \end{cases} \tag{6}$$

that is shown in Fig. 1(b). Moreover, the saturation function

$$W(v_{j-1}) = \begin{cases} v_{j-1} & \text{if} \quad v_{j-1} < v_{\max}, \\ v_{\max} & \text{if} \quad v_{j-1} \geqslant v_{\max}, \end{cases} \tag{7}$$

provides the conditions on switching between connected cruise control (CCC) mode ($v_{j-1} < v_{\max}$) where the vehicle tries to match its velocity with the predecessor's, and the normal cruise control mode ($v_{j-1} \geq v_{\max}$) where it tries to achieve the preset maximum velocity, see Fig. 1(c).

This paper will mainly focus on CCC mode when system (1) and (5) possesses the uniform flow equilibrium

$$v_{j-1}^* = v_j^* = V(h_j^*). \tag{8}$$

The objective is to design the control gains K_p, K_v such that the overall large systems (open chain or closed ring) are robust against delays due to stochastic packet drops.

The setup used in this paper allows controllers of different levels of complexity. For example, one can use more complicated connectivity topology that utilizes motion information of multiple vehicles in the neighborhood (Zhang and Orosz, 2016; Li et al., 2015), and apply different control designs (e.g., optimal control (Ge and Orosz, 2017)). However, our goal is to understand how digital effects and stochastic delays influence the dynamics of large connected vehicle systems. For this reason we consider the simplest CCC structure where each vehicle controls its motion based on the information received about the motion of the vehicle immediately ahead via V2V communication. Nevertheless the following decomposition methods can also be applied to large connected vehicle systems with more complicated connectivity topology, and the corresponding changes will be pointed out throughout the paper. We also assume that all the vehicles use the same control gains (cf. (5)), which allows us to summarize the stability results in a low dimensional parameter space. The methods presented below are applicable to systems of vehicles with different gains and it is expected that such heterogeneity can improve stability. However, investigating such effects is beyond the scope of this paper.

3. Open chain system

In this section, we consider an open chain of $(J+1)$ connected vehicles as shown in Fig. 2. Although all the vehicles are described by the same Eqs. (1) and (5), their dynamics are still not identical due to the (asynchronously changing) delays caused by stochastic packet drops. Consequently, analysis of an open chain of vehicles subject to stochastic communication delays cannot be simplified into analysis of predecessor-follower pairs as in deterministic case, but requires one to analyze the dynamics of the large stochastic connected vehicle system. In this section, a stochastic model will be built for the open chain system shown in Fig. 2, and the evolutions for the mean, second moment and covariance dynamics are derived in order to analyze the stability properties of the uniform flow equilibrium (8).

3.1. Stochastic model

The overall dynamics of the open chain system of $(J+1)$ vehicles are given by (1) and (5) for $j = 1, \ldots, J$. For simplicity of notation, the argument k of the delay $\tau_j(k)$ is not spelled out in the rest of the paper. Notice that in the time interval $t \in [t_k, t_{k+1})$, the control signal $u_j(t_{k-\tau_j})$ is a constant. Thus, one can solve the differential Eq. (1) using the input $v_0(t)$ and initial values $h(t_k)$, $v(t_k)$, which results in the discrete-time nonlinear map

$$\begin{aligned} h_1(t_{k+1}) &= h_1(t_k) - v_1(t_k)\Delta t - \frac{1}{2}u_1(t_{k-\tau_1})\Delta t^2 + \int_{t_k}^{t_{k+1}} v_0(t)\,\mathrm{d}t, \\ v_1(t_{k+1}) &= v_1(t_k) + u_1(t_{k-\tau_1})\Delta t, \\ h_j(t_{k+1}) &= h_j(t_k) + \big(v_{j-1}(t_k) - v_j(t_k)\big)\Delta t + \frac{1}{2}\Big(u_{j-1}(t_{k-\tau_{j-1}}) - u_j(t_{k-\tau_j})\Big)\Delta t^2, \\ v_j(t_{k+1}) &= v_j(t_k) + u_j(t_{k-\tau_j})\Delta t, \quad j = 2, \ldots, J. \end{aligned} \tag{9}$$

In order to analyze the stability of the stochastic system (9), we assume small variations about the equilibrium (8), i.e.,

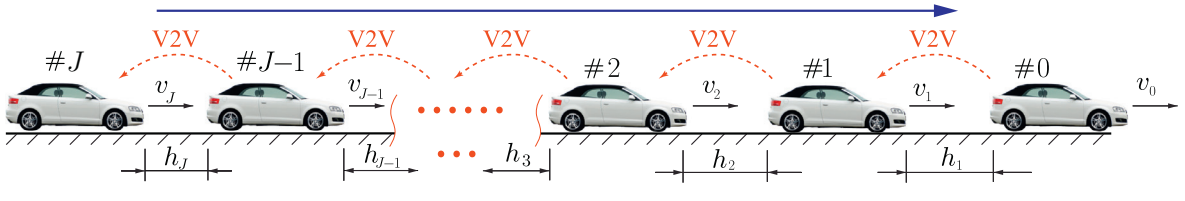

Fig. 2. An open chain of $(J+1)$ connected vehicles on a single lane. Dashed red arrows indicate the information flow through wireless communication, while the solid blue arrow indicates the direction of traffic flow.

$$\tilde{h}_j(t) = h_j(t) - h_j^*, \quad \tilde{v}_j(t) = v_j(t) - v_j^*, \quad j = 1, \ldots, J. \tag{10}$$

Moreover, Fourier's theory states that periodic signals can be represented as an infinite sum of sines and cosines, which can also be extended to absolutely integrable non-periodic signals. Henceforth, we assume sinusoidal velocity variations for the head vehicle, i.e.,

$$v_0(t) = v_0^* + v_0^{\text{amp}} \sin(\omega t) \;\Rightarrow\; \tilde{v}_0(t) = v_0^{\text{amp}} \sin(\omega t), \tag{11}$$

and $v_0(t) < v_{\max}$.

By defining the state, the output and the input as

$$x_j(k) = \begin{bmatrix} \tilde{h}_j(t_k) \\ \tilde{v}_j(t_k) \end{bmatrix}, \quad y(k) = \tilde{v}_J(t_k), \quad u(k) = \begin{bmatrix} \tilde{v}_0(t_k) \\ \tilde{v}_0^{\perp}(t_k) \end{bmatrix}, \tag{12}$$

where

$$\tilde{v}_0^{\perp}(t) = v_0^{\text{amp}} \cos(\omega t), \tag{13}$$

and using the controller (5), the linearization of (9) becomes

$$\begin{aligned}
x_1(k+1) &= \boldsymbol{a}_1 x_1(k) + \boldsymbol{a}_3 x_1(k-\tau_1) + \boldsymbol{b}_1 u(k) + \boldsymbol{b}_2 u(k-\tau_1), \\
x_2(k+1) &= \boldsymbol{a}_2 x_1(k) + \boldsymbol{a}_1 x_2(k) + \boldsymbol{a}_5 x_1(k-\tau_1) + \boldsymbol{a}_4 x_1(k-\tau_2) + \boldsymbol{a}_3 x_2(k-\tau_2) + \boldsymbol{b}_3 u(k-\tau_1), \\
x_j(k+1) &= \boldsymbol{a}_2 x_{j-1}(k) + \boldsymbol{a}_1 x_j(k) + \boldsymbol{a}_6 x_{j-2}(k-\tau_{j-1}) + \boldsymbol{a}_5 x_{j-1}(k-\tau_{j-1}) \\
&\quad + \boldsymbol{a}_4 x_{j-1}(k-\tau_j) + \boldsymbol{a}_3 x_j(k-\tau_j), \quad j = 3, \ldots, J, \\
y(k) &= c_1 x_J(k),
\end{aligned} \tag{14}$$

with the matrices given by (A.1) in Appendix A. Notice that the scalar sinusoidal input (11) that drives the continuous-time system (1) results in the vector-valued input (12) for the discrete-time system (14), where the two components are dependent. Also, notice that the input satisfies

$$u(k-r) = \mathbf{R}^r u(k), \tag{15}$$

where

$$\mathbf{R} = \begin{bmatrix} \cos(\omega\Delta t) & -\sin(\omega\Delta t) \\ \sin(\omega\Delta t) & \cos(\omega\Delta t) \end{bmatrix}. \tag{16}$$

By augmenting j-th vehicle's delayed states as

$$X_j(k) = \begin{bmatrix} x_j(k) \\ x_j(k-1) \\ \vdots \\ x_j(k-N) \end{bmatrix} \in \mathbb{R}^{2(N+1)}, \tag{17}$$

(14) can be rewritten as

$$\begin{aligned}
X_1(k+1) &= \boldsymbol{\alpha}_{1,\tau_1} X_1(k) + \boldsymbol{\beta}_{1,\tau_1} u(k), \\
X_2(k+1) &= (\boldsymbol{\alpha}_{3,\tau_1} + \boldsymbol{\alpha}_{2,\tau_2}) X_1(k) + \boldsymbol{\alpha}_{1,\tau_2} X_2(k) + \boldsymbol{\beta}_{2,\tau_1} u(k), \\
X_j(k+1) &= \boldsymbol{\alpha}_{4,\tau_{j-1}} X_{j-2}(k) + (\boldsymbol{\alpha}_{3,\tau_{j-1}} + \boldsymbol{\alpha}_{2,\tau_j}) X_{j-1}(k) + \boldsymbol{\alpha}_{1,\tau_j} X_j(k), \quad j = 3, 4, \ldots, J, \\
y(k) &= \boldsymbol{c} X_j(k),
\end{aligned} \tag{18}$$

where $\boldsymbol{\alpha}_{1,\tau_j}, \boldsymbol{\alpha}_{2,\tau_j}, \boldsymbol{\alpha}_{3,\tau_j}, \boldsymbol{\alpha}_{4,\tau_j} \in \mathbb{R}^{2(N+1)\times 2(N+1)}$ and $\boldsymbol{\beta}_{1,\tau_1}, \boldsymbol{\beta}_{2,\tau_1} \in \mathbb{R}^{2(N+1)\times 2}$ are random matrices with possible values given by (A.3) in Appendix A, and $\boldsymbol{c}$ is the output matrix given by (B.1) in Appendix B.

By defining the overall state, the input and the output

$$X(k) = \begin{bmatrix} X_1(k) \\ X_2(k) \\ \vdots \\ X_J(k) \end{bmatrix} \in \mathbb{R}^{2J(N+1)}, \quad U(k) = u(k) \in \mathbb{R}^2, \quad Y(k) = \tilde{v}_j(k) \in \mathbb{R}, \tag{19}$$

(18) can be re-written as

$$\begin{aligned}
X(k+1) &= \mathbf{A}_{\boldsymbol{\tau}} X(k) + \mathbf{B}_{\tau_1} U(k), \\
Y(k) &= \mathbf{C} X(k),
\end{aligned} \tag{20}$$

where $\boldsymbol{\tau}$ collects the random variables $\tau_1\tau_2\ldots\tau_J$, i.e., $\mathbf{A}_{\boldsymbol{\tau}}$ denotes $\mathbf{A}_{\tau_1\tau_2\ldots\tau_J}$. The possible values for $\mathbf{A}_{\boldsymbol{\tau}}$ and $\mathbf{B}_{\tau_1}$ are given by (B.4) in Appendix B, and the output matrix $\mathbf{C}$ is given in (B.3) in Appendix B.

We remark that there is another way to rewrite (14) into state space form by inserting different vehicles' states into a vector first, and then augmenting the resulting states over time. However, the way presented above better supports physical intuition and make the forthcoming calculations technically less challenging.

3.2. Dynamics for the mean, second moment and covariance

In order to find stability conditions, the mean, the second moment and the covariance dynamics need to be derived in the same way as in (Qin et al., 2017). With the IID assumption of $\boldsymbol{\tau}(k)$ explained in Section 2, one can obtain the PDF-s of $\mathbf{A}_{\boldsymbol{\tau}}$ and $\mathbf{B}_{\tau_1}$ as

$$f_{\mathbf{A}_{\boldsymbol{\tau}}}(\mathbf{A})=\sum_{\boldsymbol{r}=1}^{\infty}w_{\boldsymbol{r}}\delta(\mathbf{A}-\mathbf{A}_{\boldsymbol{r}}),\quad f_{\mathbf{B}_{\tau_1}}(\mathbf{B})=\sum_{r_1=1}^{\infty}w_{r_1}\delta(\mathbf{B}-\mathbf{B}_{r_1}),\tag{21}$$

respectively, where $\boldsymbol{r}$ is the set of realization for $\boldsymbol{\tau}$, i.e., $\mathbf{A}_{\boldsymbol{r}}$ denotes $\mathbf{A}_{r_1r_2\ldots r_J}$ and $\sum_{\boldsymbol{r}=1}^{N}w_{\boldsymbol{r}}$ denotes $\sum_{r_1=1}^{N}\sum_{r_2=1}^{N}\cdots\sum_{r_J=1}^{N}w_{r_1}w_{r_2}\cdots w_{r_J}$. Notice that $\mathbf{A}_{\boldsymbol{\tau}}$ and $X(k)$ are mutually independent, which is also the case for $\mathbf{B}_{\tau_1}$ and $X(k)$.

The mean values of state variables can be defined as

$$\bar{X}(k)=\mathbb{E}[X(k)]\in\mathbb{R}^{2J(N+1)},\quad \bar{Y}(k)=\mathbb{E}[Y(k)]\in\mathbb{R},\tag{22}$$

where $\mathbb{E}[\cdot]$ denotes the expected value. By taking expected value of both sides in (20) with the PDF-s (21) and using independency between variables, one can derive the mean dynamics

$$\begin{aligned}\bar{X}(k+1)&=\bar{\mathbf{A}}\bar{X}(k)+\bar{\mathbf{B}}U(k),\\ \bar{Y}(k)&=\bar{\mathbf{C}}\bar{X}(k),\end{aligned}\tag{23}$$

where the state matrix, the input matrix and the output matrix are the expected values of corresponding matrices given in (B.4) in Appendix B, i.e.,

$$\bar{\mathbf{A}}=\sum_{\boldsymbol{r}=1}^{N}w_{\boldsymbol{r}}\mathbf{A}_{\boldsymbol{r}},\quad \bar{\mathbf{B}}=\sum_{r_1=1}^{N}w_{r_1}\mathbf{B}_{r_1},\quad \bar{\mathbf{C}}=\mathbf{C},\tag{24}$$

and their explicit expressions are spelled out in (B.5) in Appendix B.

Similarly, the second moments of state variables can be defined as

$$\hat{X}(k)=\mathbb{E}[X(k)\otimes X(k)]\in\mathbb{R}^{2^2J^2(N+1)^2},\quad \hat{Y}(k)=\mathbb{E}[Y(k)\otimes Y(k)]\in\mathbb{R},\tag{25}$$

using Kronecker product. By taking expected value with the PDF-s (21) and using independency between variables, one can obtain the second moment dynamics

$$\begin{aligned}\hat{X}(k+1)&=\Big(\sum_{\boldsymbol{r}=1}^{N}w_{\boldsymbol{r}}\mathbf{A}_{\boldsymbol{r}}\otimes\mathbf{A}_{\boldsymbol{r}}\Big)\hat{X}(k)+\Big(\sum_{\boldsymbol{r}=1}^{N}w_{\boldsymbol{r}}\mathbf{A}_{\boldsymbol{r}}\otimes\mathbf{B}_{\boldsymbol{r}}\Big)(\bar{X}(k)\otimes U(k))\\&\quad+\Big(\sum_{\boldsymbol{r}=1}^{N}w_{\boldsymbol{r}}\mathbf{B}_{\boldsymbol{r}}\otimes\mathbf{A}_{\boldsymbol{r}}\Big)(U(k)\otimes\bar{X}(k))+\Big(\sum_{\boldsymbol{r}=1}^{N}w_{\boldsymbol{r}}\mathbf{B}_{\boldsymbol{r}}\otimes\mathbf{B}_{\boldsymbol{r}}\Big)(U(k)\otimes U(k)),\\ \hat{Y}(k)&=(\mathbf{C}\otimes\mathbf{C})\hat{X}(k).\end{aligned}\tag{26}$$

Finally, the covariance can be defined as

$$\begin{aligned}\bar{\bar{X}}(k)&=\mathbb{E}\big[\big(X(k)-\bar{X}(k)\big)\otimes\big(X(k)-\bar{X}(k)\big)\big]\in\mathbb{R}^{2^2J^2(N+1)^2},\\ \bar{\bar{Y}}(k)&=\mathbb{E}\big[\big(Y(k)-\bar{Y}(k)\big)\otimes\big(Y(k)-\bar{Y}(k)\big)\big]\in\mathbb{R},\end{aligned}\tag{27}$$

and it can be shown that

$$\bar{\bar{X}}(k)=\mathbb{E}[X(k)\otimes X(k)]-\bar{X}(k)\otimes\bar{X}(k),\quad \bar{\bar{Y}}(k)=\mathbb{E}[Y(k)\otimes Y(k)]-\bar{Y}(k)\otimes\bar{Y}(k).\tag{28}$$

Thus, using (23) and (26), one can obtain the covariance dynamics

$$\begin{aligned}\bar{\bar{X}}(k+1)&=\bar{\bar{\mathbf{A}}}\bar{\bar{X}}(k)+\bar{\bar{\mathbf{K}}}_1(\bar{X}(k)\otimes\bar{X}(k))+\bar{\bar{\mathbf{K}}}_2(\bar{X}(k)\otimes U(k))\\&\quad+\bar{\bar{\mathbf{K}}}_3(U(k)\otimes\bar{X}(k))+\bar{\bar{\mathbf{K}}}_4(U(k)\otimes U(k)),\\ \bar{\bar{Y}}(k)&=\bar{\bar{\mathbf{C}}}\bar{\bar{X}}(k),\end{aligned}\tag{29}$$

where

$$\bar{\bar{\mathbf{A}}} = \sum_{r=1}^{N} w_r \mathbf{A}_r \otimes \mathbf{A}_r, \quad \bar{\bar{\mathbf{C}}} = \mathbf{C} \otimes \mathbf{C},$$
$$\bar{\bar{\mathbf{K}}}_1 = \sum_{r=1}^{N} w_r \mathbf{A}_r \otimes \mathbf{A}_r - \bar{\mathbf{A}} \otimes \bar{\mathbf{A}}, \quad \bar{\bar{\mathbf{K}}}_2 = \sum_{r=1}^{N} w_r \mathbf{A}_r \otimes \mathbf{B}_r - \bar{\mathbf{A}} \otimes \bar{\mathbf{B}}, \tag{30}$$
$$\bar{\bar{\mathbf{K}}}_3 = \sum_{r=1}^{N} w_r \mathbf{B}_r \otimes \mathbf{A}_r - \bar{\mathbf{B}} \otimes \bar{\mathbf{A}}, \quad \bar{\bar{\mathbf{K}}}_4 = \sum_{r=1}^{N} w_r \mathbf{B}_r \otimes \mathbf{B}_r - \bar{\mathbf{B}} \otimes \bar{\mathbf{B}},$$

cf. (23), (24). The time evolutions of the mean and the covariance are described by the nonlinear system (23) and (29) such that (29) is driven by (23).

3.3. Plant stability and string stability

Plant stability and string stability are often used to characterize traffic systems. In the predecessor-follower pair system, plant stability characterizes the follower's capability of approaching a constant desired velocity dictated by the predecessor. In an open chain system, plant stability indicates whether all the following vehicles are able to approach the constant desired velocity dictated by the head vehicle. The importance of plant stability lies in the fact that plant unstable traffic systems can lead to vehicle crashes. Fig. 3 shows two simulation results of an open chain of $(15+1)$ connected vehicles for different $(K_\mathrm{v}, K_\mathrm{p})$ gains for the parameters $v_{\max} = 30$ [m/s], $h_{\mathrm{st}} = 5$ [m], $h_{\mathrm{go}} = 35$ [m], $v_0^* = 15$ [m/s], $\Delta t = 0.1$ [s] (cf. (6) and (8)), which will be kept the same throughout the whole paper. Here, the packet delivery ratio is $p = 0.6$ and only the velocities of every third vehicle are shown. Fig. 3(a) shows the time profiles for a simulation demonstrating plant stability as all the velocities approach the head vehicle's velocity despite the initial perturbations and stochastic packet drops. Thus, one can say that this realization is plant stable. However, to check whether this pair of $(K_\mathrm{v}, K_\mathrm{p})$ gains is plant stable in the stochastic sense, one has to investigate all the possible realizations (that is clearly not feasible via simulations). Fig. 3(b) shows the time profiles for one plant unstable simulation, where the vehicles are unable to maintain the same constant velocity prescribed by the head vehicle.

String stability in the predecessor-follower system characterizes the follower's capability of attenuating fluctuations introduced by the predecessor. For an open chain vehicle system, string stability requires attenuation of fluctuations between the head vehicle and the tail vehicle (Zhang and Orosz, 2016). String unstable traffic systems may trigger stop-and-go motion, sometimes referred to as phantom traffic jams. Fig. 4 shows three simulation results for an open chain of $(200+1)$ connected vehicles when the head vehicle is introducing a sinusoidal fluctuation into the system and the packet delivery ratio is $p = 0.4$. Here, only the velocities of every 40-th vehicles are shown, and the other parameters remain the same as those for Fig. 3. It can be seen from Fig. 4(a) that the fluctuation introduced by the head vehicle is attenuated by all the vehicles shown in the figure, including the tail vehicle. However, similar to the argument for plant stability, to check whether this pair of $(K_\mathrm{v}, K_\mathrm{p})$ gains is string stable in the stochastic sense, one has to investigate all the possible realizations for all the possible excitation frequencies. Fig. 4(b, c) show the time profiles for two string unstable scenarios, where the tail vehicle is unable to attenuate the fluctuation introduced by the head vehicle. In Fig. 4(b), the fluctuation introduced by the head vehicle propagates upstream in the traffic flow and is amplified every now and then. Such fluctuations deteriorate driving comfort and fuel economy. Because of the stochasticity in packet drops, one may notice that the fluctuations are not perfectly sinusoidal. Whereas, in Fig. 4(c), the single-frequency fluctuation introduced by the head vehicle triggers more fluctuations with different frequencies in the following vehicles due to the stochastic nature in the packet delivery, which

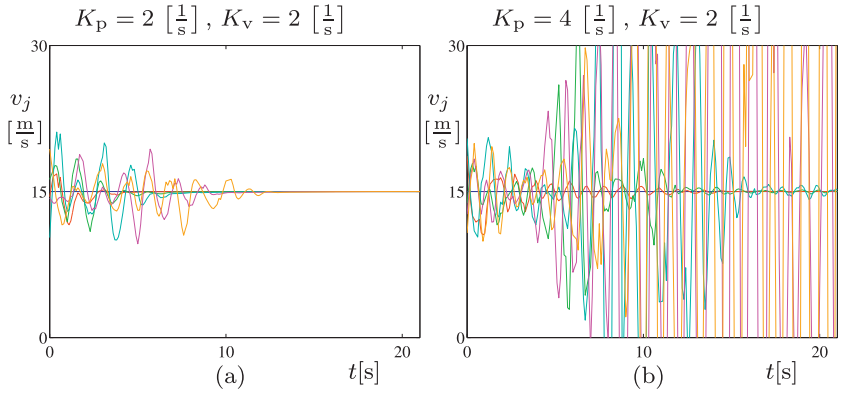

Fig. 3. Plant stability simulations for an open chain of $(15+1)$ connected vehicles for different $(K_\mathrm{v}, K_\mathrm{p})$ gains as indicated. The blue curves represent the velocity v_0 of the head vehicle while the red, green, cyan, magenta and orange curves represent the velocities v_3, v_6, v_9, v_{12}, v_{15}, respectively. (a) Plant stable. (b) Plant unstable.

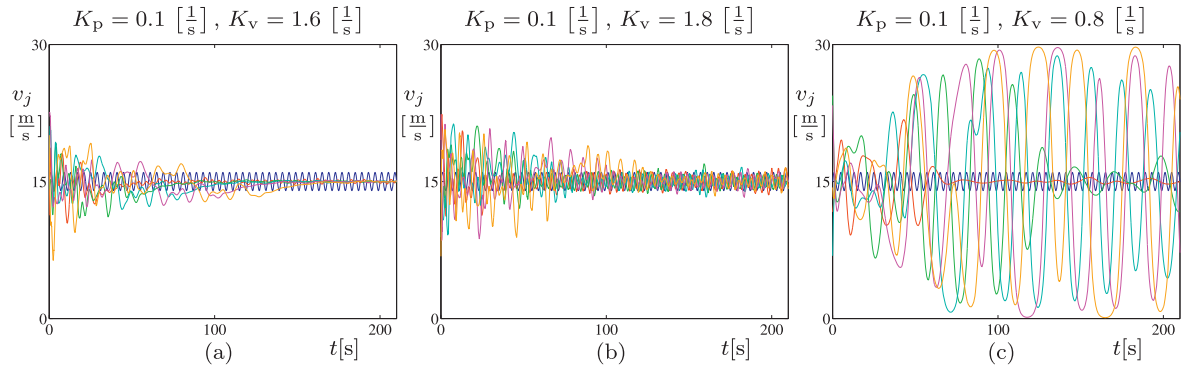

Fig. 4. String stability simulations for an open chain of $(200+1)$ connected vehicles for different (K_v, K_p) gains as indicated. The blue curves represent the velocity v_0 of the head vehicle while the red, green, cyan, magenta and orange curves represent the velocities v_{40}, v_{80}, v_{120}, v_{160}, v_{200}, respectively. (a) String stable. (b) String unstable. (c) String unstable.

gives rise to stop-and-go traffic waves traveling upstream. In the controller design, we need to assure string stability in order to prevent such phenomena.

In this section, we derive and simplify conditions on both plant stability and string stability for the dynamics of the mean (23) and the covariance (29) for open chains subject to stochastic packet drops.

3.3.1. Plant stability

In the following, we will evaluate plant stability for both mean and second moment dynamics. On one hand, plant stability for the mean dynamics requires that the mean values of all the followers' velocities approach the head vehicle's velocity. This is a necessary condition for the plant stability of the stochastic system (20). On the other hand, the plant stability of the second moment dynamics (26) (or the covariance dynamics (29)) requires that the variances of all the followers' velocities converge to zero. This provides a sufficient condition for the (almost sure) plant stability (Appendix D) of the stochastic system (20). Therefore, we will derive conditions on plant stability for the mean dynamics and second moment dynamics. In order to test plant stability, we need to set the head vehicle's velocity to be a constant, i.e.,

$$v_0^{\text{amp}} = 0 \ \Rightarrow\ v_0(t) \equiv v_0^*, \quad \tilde{v}_0(t) \equiv 0, \quad \tilde{v}_0^{\perp}(t) \equiv 0, \tag{31}$$

in (11) and (13) or $u(k) \equiv 0$ in (12).

For plant stability of the mean dynamics $\bar{X}(k+1) = \bar{\mathbf{A}}\bar{X}(k)$ (cf. (23) with $U(k) \equiv 0$), all the eigenvalues of the matrix $\bar{\mathbf{A}}$ must lie within the unit circle in the complex plane. By observing (B.5) in Appendix B, one may notice that the eigenvalues of $\bar{\mathbf{A}}$ consist of all the eigenvalues of $\bar{\boldsymbol{\alpha}}_1$, each with multiplicity J, cf. (A.4). In order to assure that the mean dynamics are plant stable, we need to make sure that all the eigenvalues of the matrix $\bar{\boldsymbol{\alpha}}_1$ lie within the unit circle in the complex plane. Finding the corresponding stability boundaries analytically in the (K_v, K_p)-plane is very difficult, so we use the bisection method (Qin et al., 2017; Bachrathy and Stépán, 2012) in order to trace the boundaries. We remark that those plant stability boundaries depend on the parameters $(K_p, K_v, p, v_0^*, \Delta t)$, but independent of the number of cars J.

In (Qin et al., 2017), it was shown that stability of the second moment dynamics and stability of the covariance dynamics are equivalent when the mean dynamics are stable. Consequently, only the plant stability for the second moment dynamics is discussed here. Similar to the mean dynamics, to ensure plant stability of the second moment dynamics $\hat{\bar{X}}(k+1) = \bar{\bar{\mathbf{A}}}\hat{\bar{X}}(k)$ (cf. (26) with $U(k) \equiv 0$ and $\bar{\bar{\mathbf{A}}}$ defined in (30)), all the eigenvalues of the matrix $\bar{\bar{\mathbf{A}}}$ must lie within the unit circle in the complex plane.

While solving this problem, we are faced with three issues. The first one lies in the construction of the possible values for the Kronecker product $\mathbf{A}_r \otimes \mathbf{A}_r$ due to its huge dimension $2^2J^2(N+1)^2$, where J is the number of vehicles and N is the

Table 1
Effort characteristics of the matrix $\bar{\bar{\mathbf{A}}}$ for $(J+1)$ connected vehicles and $N = 6$.

	J	3	9	15	21	27
Before Decomposition	$2^2J^2(N+1)^2$	1764	15876	44100	86436	142884
	storage (GB)	0.023	1.878	14.490	55.665	152.110
	N^J	216	1.1×10^7	4.7×10^{11}	2.2×10^{16}	1.0×10^{21}
After Decomposition	$2^2(N+1)^2$	196	196	196	196	196
	storage (GB)	<0.001	<0.001	<0.001	<0.001	<0.001
	N	6	6	6	6	6

maximum delay. Table 1 shows how this dimension changes while varying numbers of cars J when the maximum delay is $N = 6$. It also shows how much RAM space is needed to store one of its possible values, given that each entry takes 8-byte storage space. The second issue is the difficulty in enumerating all the N^J possible values of $\mathbf{A_r} \otimes \mathbf{A_r}$, when calculating the weighted sum in (30). As J increases, N^J increases dramatically, cf. Table 1. The third and the most critical issue is to determine plant stability changes while varying parameters, that is, frequent eigenvalue calculations on huge matrices with high multiplicity of eigenvalues. The appearance of high multiplicity in eigenvalues will be shown later. In this case accuracy of eigenvalues degrades significantly as the size of the matrix and the eigenvalue multiplicity increase; see (Trefethen and Bau, 1997). Henceforth, decomposition must be done to assure scalability of computations on plant stability.

The decomposition procedure outlined in the supplemental document relies on applying properties of the Kronecker product (Laub, 2005; Olson et al., 2014; Loan, 2000) and using perfect shuffle (Loan, 2000; Davio, 1981). This allows us to transform matrix $\bar{\bar{\mathbf{A}}}$ to a block diagonal matrix $\tilde{\bar{\mathbf{A}}}$, that can be constructed using a weighted sum of N Kronecker products (rather than N^J). Also, instead of enumerating $\mathbf{A_r} \otimes \mathbf{A_r}$, we enumerate $\boldsymbol{\alpha}_{i_1,\tau_{j_1}} \otimes \boldsymbol{\alpha}_{i_2,\tau_{j_2}}$, cf. (A.3) and (B.4), that is, the matrix dimension decreases from size $2^2J^2(N+1)^2$ to size $2^2(N+1)^2$. Table 1 also shows some effort characteristics needed to create $\tilde{\bar{\mathbf{A}}}$. Due to the fact that the eigenvalues of similar matrices are the same, the eigenvalues of matrix $\bar{\bar{\mathbf{A}}}$ are the same as the eigenvalues of matrix $\tilde{\bar{\mathbf{A}}}$. In particular, they are given by the eigenvalues of

$$\hat{\bar{\boldsymbol{\alpha}}}_{11} = \bar{\boldsymbol{\alpha}}_1 \otimes \bar{\boldsymbol{\alpha}}_1, \tag{32}$$

each with multiplicity $J(J-1)$, and the eigenvalues of

$$\bar{\bar{\boldsymbol{\alpha}}}_{11} = \sum_{l=1}^{N} w_l \boldsymbol{\alpha}_{1,l} \otimes \boldsymbol{\alpha}_{1,l}, \tag{33}$$

each with multiplicity J, cf. (A.3).

Moreover, when plant stability of the second moment is concerned, plant stability of the mean dynamics must be guaranteed first. That is, all the eigenvalues of matrix $\bar{\boldsymbol{\alpha}}_1$ lie inside the unit circle in the complex plane, which yields that all the eigenvalues of matrix $\hat{\bar{\boldsymbol{\alpha}}}_{11}$ also lie inside the unit circle according to the properties of Kronecker product (Laub, 2005). Thus, the plant stability condition of the second moment is simplified to assure that the eigenvalues of $\bar{\bar{\boldsymbol{\alpha}}}_{11}$ lie inside the unit circle in the complex plane. Notice that $\bar{\bar{\boldsymbol{\alpha}}}_{11}$ is the weighted sum of N Kronecker products of matrices with dimension $2^2(N+1)^2$ and that $\bar{\bar{\boldsymbol{\alpha}}}_{11}$ is independent of J, that is, the plant stability condition does not depend on the number of cars. Similar to the argument for mean dynamics, the plant stability boundaries of the second moment dynamics still depend on the parameters $(K_\mathrm{p}, K_\mathrm{v}, p, v_0^*, \Delta t)$.

Fig. 5 shows the plant stability diagrams in the $(K_\mathrm{v}, K_\mathrm{p})$-plane for different packet delivery ratios. The inlets are the probability distributions of discrete stochastic delay given by (2). The red lines and red curves correspond to plant stability boundaries for the mean dynamics. The regions enclosed by these curves, i.e., the union of the light red and light blue shaded regions, are the mean plant stable regions. The blue lines and blue curves correspond to plant stability boundaries for the second moment dynamics. The light blue shaded regions enclosed by them are the second moment plant stable regions. It can be seen that the difference between plant stability boundaries for the mean dynamics and second moment dynamics is increasing while the successful packet delivery ratio p decreases, i.e., the second moment dynamics plays an important role when packet drops happen frequently in the V2V communication.

3.3.2. String stability

In this part, we follow the method and extend the notion presented in (Qin et al., 2017) to determine string stability for the mean and covariance dynamics of the open chain system using transfer functions, which allow us to evaluate the behavior of the open chain under stochastic delay variations. In order to test string stability, we consider the periodic input $\tilde{v}_0(t)$

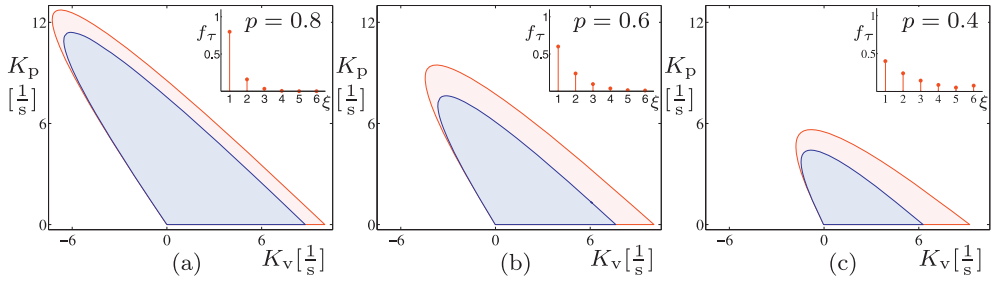

Fig. 5. Plant stability diagrams for an open chain of $(J+1)$ connected vehicles in the $(K_\mathrm{v}, K_\mathrm{p})$-plane for different values of packet delivery ratio p. The corresponding delay distributions (2) are plotted on each panel as inlets.

given in (11) and the output $\tilde{v}_J(t)$ of the tail vehicle. After discretizing time (cf. (12) and (14)), we obtain two discrete inputs $\tilde{v}_0(k)$ and $\tilde{v}_0^{\perp}(k)$, and one discrete output $\tilde{v}_J(k)$. We can derive the amplification ratio and phase lag for the mean dynamics as

$$\bar{M}(\omega) = |\bar{\Gamma}(\mathrm{e}^{\mathrm{j}\omega\Delta t})|, \quad \bar{\psi}(\omega) = \angle\bar{\Gamma}(\mathrm{e}^{\mathrm{j}\omega\Delta t}), \tag{34}$$

where the transfer function

$$\bar{\Gamma}(z) = \bar{\mathbf{C}}\big(z\bar{\mathbf{I}} - \bar{\mathbf{A}}\big)^{-1}\bar{\mathbf{B}}\bar{\mathbf{E}} \tag{35}$$

is obtained by applying Z transform to (23), and

$$\bar{\mathbf{E}} = [\,1 \quad \mathrm{j}\,]^{\mathrm{T}} \tag{36}$$

is used to sum up the effects of two inputs. Notice that $\bar{\mathbf{A}}$ (cf. (B.5)) is a block lower triangular matrix and $\bar{\mathbf{B}}$ (cf. (B.5)) has many zero elements, the calculation of transfer function of mean dynamics can be further simplified into calculation of matrices with much lower dimensions using block matrix inverse (Henderson and Searle, 1981). Such simplification is explained in detail in the supplemental document.

The string stability condition for mean dynamics is given by

$$\sup_{\omega>0} \bar{M}(\omega) < 1. \tag{37}$$

We remark that $\bar{M}(\omega)$ also depends on the parameters $(K_\mathrm{p}, K_\mathrm{v}, p, v_0^*, \Delta t, J)$. Again it is difficult to find the stability boundaries analytically, so we trace them numerically using the bisection method.

Fig. 6 shows string stability diagrams for the mean dynamics in the $(K_\mathrm{v}, K_\mathrm{p})$-plane for different values of packet delivery ratio p and numbers of cars J. The green lines and curves correspond to the mean string stability boundaries, while the light green shaded regions enclosed by them are the mean string stable regions. (The orange lines and curves, and the light orange shaded regions will be explained later.) Note that the mean string stable regions must be embedded in the corresponding mean plant stable regions, because plant stability is the prerequisite for string stability. In each panel, the boundaries corresponding to $J = 3, 9, 15, 21, 27$, are plotted together such that the more vehicles there are, the darker the green boundary is. However, the differences between different J-s are very small and possibly caused by numerical errors. In other words, the mean string stability boundaries seem to be independent of the number of cars. Thus, the mean string stability condition for open chain systems with fewer numbers of cars gives a very good estimate of that for the case with large numbers of cars.

To elaborate more on this, we use $\bar{M}(\omega; J)$ to spell out its dependence on the number of cars J. Suppose the amplification ratio of the mean dynamics from the head vehicle to the first vehicle is $\bar{M}(\omega; 1)$ where $\omega > 0$, then it can be used to approximate the amplification ratio from the j-th vehicle to the $(j+1)$-th vehicle if we neglect the difference between the perfect sinusoidal fluctuations in the head vehicle and triggered fluctuations in the j-th vehicle. This implies that

$$\bar{M}(\omega; J) \approx \bar{M}(\omega; 1)^J, \quad \omega > 0, \tag{38}$$

and the approximation of (37) becomes

$$\sup_{\omega>0} \bar{M}(\omega; 1)^J < 1 \;\Rightarrow\; \sup_{\omega>0} \bar{M}(\omega; 1) < 1, \tag{39}$$

since the amplification ratio is positive. That is, the mean string stability is independent of the number of cars J.

In order to derive string stability conditions for the covariance dynamics (29), only the steady state response to the sinusoidal input (10) is needed. However, the covariance dynamics (29) do not provide a direct input-output relationship as the mean dynamics (23) do, because the covariance dynamics (29) are nonlinear and also contain terms driven by the mean dynamics (23). To simplify the analysis, we assume that the mean dynamics are plant stable and already at steady state, that is,

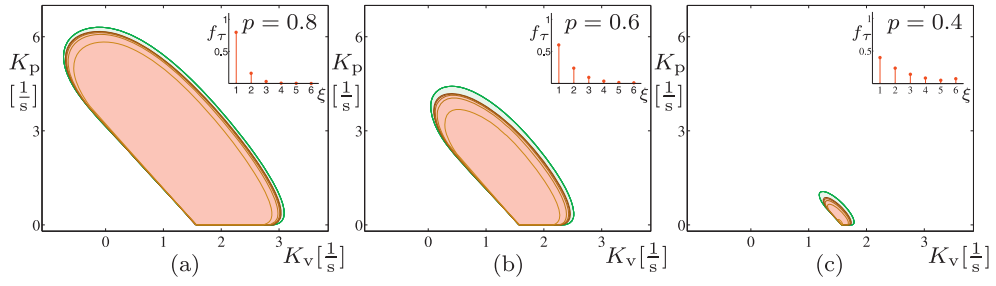

Fig. 6. Mean string stability and 1σ string stability diagrams for an open chain of $(J+1)$ connected vehicles in the $(K_\mathrm{v}, K_\mathrm{p})$-plane for different values of packet delivery ratio p. Each panel plots all the boundaries for mean string stability corresponding to $J = 3, 9, 15, 21, 27$ from light green to dark green curves, and 1σ string stability corresponding to $J = 3, 9, 15, 21, 27$ from light orange to dark orange curves, respectively.

$$\bar{X}(k) = \mathbf{Q}U(k), \tag{40}$$

where $\mathbf{Q}$ satisfies

$$\mathbf{Q} - \bar{\mathbf{A}}\mathbf{Q}\mathbf{R} = \bar{\mathbf{B}}\mathbf{R}, \tag{41}$$

which can be obtained by substituting Eq. (40) into mean dynamics (23) and using the property (15).

Substituting (40) into (29) yields the simplified covariance dynamics

$$\begin{aligned} \bar{\bar{X}}(k+1) &= \bar{\bar{\mathbf{A}}}\,\bar{\bar{X}}(k) + \bar{\bar{\mathbf{B}}}\,\bar{\bar{U}}(k), \\ \bar{\bar{Y}}(k) &= \bar{\bar{\mathbf{C}}}\,\bar{\bar{X}}(k), \end{aligned} \tag{42}$$

where

$$\bar{\bar{U}}(k) = U(k) \otimes U(k), \tag{43}$$

and $\bar{\bar{\mathbf{A}}}$ and $\bar{\bar{\mathbf{C}}}$ are given by (30), while

$$\bar{\bar{\mathbf{B}}} = \bar{\bar{\mathbf{K}}}_1(\mathbf{Q} \otimes \mathbf{Q}) + \bar{\bar{\mathbf{K}}}_2(\mathbf{Q} \otimes \mathbf{I}) + \bar{\bar{\mathbf{K}}}_3(\mathbf{I} \otimes \mathbf{Q}) + \bar{\bar{\mathbf{K}}}_4. \tag{44}$$

Similar to $\bar{\bar{\mathbf{A}}}$, the matrices $\bar{\bar{\mathbf{K}}}_1, \bar{\bar{\mathbf{K}}}_2, \bar{\bar{\mathbf{K}}}_3$ and $\bar{\bar{\mathbf{K}}}_4$ are difficult to construct due to enormous enumeration of possibilities and huge sizes. Therefore, decomposition based on block matrix calculation of Kronecker product and perfect shuffle can be used to simplify the calculations; see supplemental document for more details.

Recall that $\bar{Y}(k) = \mathbb{E}[\tilde{v}_J(k)] \in \mathbb{R}$ and $\bar{\bar{Y}}(k) = \mathbb{E}[\tilde{v}_J^2(k)] - \mathbb{E}[\tilde{v}_J(k)]^2 \in \mathbb{R}$ are the mean value and variance of the velocity $\tilde{v}_J(k)$ of the tail vehicle. If we define

$$\mu = \bar{Y}_{\mathrm{ss}}(k), \quad \sigma^2 = \bar{\bar{Y}}_{\mathrm{ss}}(k), \tag{45}$$

as the mean and variance of $\tilde{v}_J(k)$ at steady state, respectively, then the probability of $\tilde{v}_J(k)$ being outside the window $[\mu - n\sigma, \mu + n\sigma]$, $n \in \mathbb{R}^+$ is rather small when $n \geq 1$ according to Chebyshev's inequality (Feller, 1950). Therefore, the following definition is proposed.

Definition 1. The system is *$n\sigma$ string stable* if the input $\tilde{v}_0(k)$ is attenuated such that

$$|\mu \pm n\sigma| < v_0^{\mathrm{amp}}, \quad k = 0, 1, 2, \ldots \tag{46}$$

Note that when $n = 0$, the $n\sigma$ string stability condition gives the mean string stability condition. One may notice that as n is increased, $n\sigma$ string stability condition gets stronger since fewer trajectories are allowed to be outside the interval $[\mu - n\sigma, \mu + n\sigma]$. Thus, mean string stability gives the weakest condition and $n\sigma$ string stability with $n \geq 1$ implies that mean string stability is satisfied. Also, we remark that the natural choice of n is $n = 1$, and in Section 5 we will use stability charts to demonstrate that 1σ string stability of the open chain system is comparable to the second moment stability of the closed ring system.

From linear system theory, the steady state of the mean value is

$$\mu = v_0^{\mathrm{amp}} \bar{M}(\omega) \sin\left(k\omega\Delta t + \bar{\psi}(\omega)\right), \tag{47}$$

cf. (34). Thus, the steady state of the variance is needed. By substituting the input (12) into (43), one may notice that the input $\bar{\bar{U}}(k)$ can be separated into a constant part and a harmonic excitation part, i.e.,

$$\bar{\bar{U}}(k) = \bar{\bar{U}}_0 + \bar{\bar{U}}_1(k), \tag{48}$$

where

$$\bar{\bar{U}}_0 = \frac{1}{2}\left(v_0^{\mathrm{amp}}\right)^2 \bar{\bar{u}}_0, \quad \bar{\bar{U}}_1(k) = \frac{1}{2}\left(v_0^{\mathrm{amp}}\right)^2 \bar{\bar{u}}_1(k), \tag{49}$$

and

$$\bar{\bar{u}}_0 = \begin{bmatrix} 1 \\ 0 \\ 0 \\ 1 \end{bmatrix}, \quad \bar{\bar{u}}_1(k) = \begin{bmatrix} -\cos(2k\omega\Delta t) \\ \sin(2k\omega\Delta t) \\ \sin(2k\omega\Delta t) \\ \cos(2k\omega\Delta t) \end{bmatrix}. \tag{50}$$

According to superposition principle, the particular solution of the linear system (42) is the sum of particular solution $\bar{\bar{Y}}_0$ to $\bar{\bar{U}}_0$ and particular solution $\bar{\bar{Y}}_1(k)$ to $\bar{\bar{U}}_1(k)$. For input $\bar{\bar{U}}_0$, the response of the system (42) is given by

$$\bar{\bar{Y}}_0 = \left(v_0^{\mathrm{amp}}\right)^2 \bar{\bar{M}}_0(\omega), \tag{51}$$

with

$$\bar{\bar{M}}_0(\omega) = \frac{1}{2}\bar{\bar{\mathbf{C}}}\left(\bar{\bar{\mathbf{I}}} - \bar{\bar{\mathbf{A}}}\right)^{-1}\bar{\bar{\mathbf{B}}}\bar{\bar{u}}_0. \tag{52}$$

We remark that $\bar{\bar{M}}_0(\omega)$ depends on ω because matrix $\bar{\bar{\mathbf{B}}}$ depends on ω, cf. (A.1), (A.4), (B.5), (30), (44). For $\bar{\bar{U}}_1(k)$, similar to mean dynamics, taking the Z transform of (42) and summing the contributions of each individual inputs of $\bar{\bar{u}}_1(k)$ in (50), we obtain the corresponding steady state output

$$\bar{\bar{Y}}_{1,\mathrm{ss}}(k) = \left(v_0^{\mathrm{amp}}\right)^2\bar{\bar{M}}_1(\omega)\sin\left(2k\omega\Delta t + \bar{\bar{\psi}}(\omega)\right). \tag{53}$$

Here, the amplification ratio and phase lag are

$$\bar{\bar{M}}_1(\omega) = |\bar{\bar{\Gamma}}(\mathrm{e}^{\mathrm{j}\omega\Delta t})|, \quad \bar{\bar{\psi}}(\omega) = \angle\bar{\bar{\Gamma}}(\mathrm{e}^{\mathrm{j}\omega\Delta t}), \tag{54}$$

where

$$\bar{\bar{\Gamma}}(z) = \frac{1}{2}\bar{\bar{\mathbf{C}}}\left(z\bar{\bar{\mathbf{I}}} - \bar{\bar{\mathbf{A}}}\right)^{-1}\bar{\bar{\mathbf{B}}}\bar{\bar{\mathbf{E}}}, \tag{55}$$

and

$$\bar{\bar{\mathbf{E}}} = [\,-\mathrm{j} \quad 1 \quad 1 \quad \mathrm{j}\,]^{\mathrm{T}}. \tag{56}$$

Therefore, the superposition principle yields that the steady state response to (48) is

$$\sigma^2 = \bar{\bar{Y}}_0 + \bar{\bar{Y}}_{1,\mathrm{ss}}(k) = \left(v_0^{\mathrm{amp}}\right)^2\left(\bar{\bar{M}}_0(\omega) + \bar{\bar{M}}_1(\omega)\sin\left(2k\omega\Delta t + \bar{\bar{\psi}}(\omega)\right)\right). \tag{57}$$

The non-negativity of the variance yields that $\bar{\bar{M}}_0(\omega) \geqslant \bar{\bar{M}}_1(\omega)$. Hitherto we can calculate

$$\mu \pm n\sigma = v_0^{\mathrm{amp}}\left[\bar{M}(\omega)\sin\left(k\omega\Delta t + \bar{\psi}(\omega)\right) \pm n\sqrt{\bar{\bar{M}}_0(\omega) + \bar{\bar{M}}_1(\omega)\sin\left(2k\omega\Delta t + \bar{\bar{\psi}}(\omega)\right)}\right], \tag{58}$$

which is a periodic function with period $T = 2\pi/(\omega\Delta t)$. Thus, the total amplification ratio becomes

$$\bar{\bar{M}}(\omega) = \max_{0\leqslant k\leqslant T}\left\{\left|\bar{M}(\omega)\sin\left(k\omega\Delta t + \bar{\psi}(\omega)\right) \pm n\sqrt{\bar{\bar{M}}_0(\omega) + \bar{\bar{M}}_1(\omega)\sin\left(2k\omega\Delta t + \bar{\bar{\psi}}(\omega)\right)}\right|\right\}, \tag{59}$$

and the condition for $n\sigma$ string stability is given by

$$\sup_{\omega>0}\bar{\bar{M}}(\omega) < 1. \tag{60}$$

Again we remark that $\bar{\bar{M}}_0(\omega)$, $\bar{\bar{M}}_1(\omega)$ and $\bar{\bar{M}}(\omega)$ depend on the parameters $(K_{\mathrm{p}}, K_{\mathrm{v}}, p, v_0^*, \Delta t, J)$. The corresponding boundaries can be found numerically by bisection method.

Fig. 6 also shows the 1σ string stability diagrams in the $(K_{\mathrm{v}}, K_{\mathrm{p}})$-plane for different values of packet delivery ratio p and number of cars J. The orange lines and curves correspond to the 1σ string stability boundaries for an open chain of different number of cars such that the more vehicles there are, the darker the orange boundary is. The light orange shaded regions are the 1σ string stable regions for an open chain of $J = 27$ cars. Indeed, the 1σ string stable regions are embedded in the corresponding covariance plant stable regions. Fig. 6 illustrates that the 1σ string stable regions expand as the number of vehicles J increases. Also, the 1σ string stable region converges to a limit as the number of vehicles J goes to infinity. If one can succeed in obtaining this limit, that will be the necessary conditions of 1σ string stable conditions for an open chain of any number of cars. However, this is computationally infeasible and simplification is rather difficult. Thus, we take 1σ string stability for an open chain of the largest number of vehicles that we can calculate so far, i.e., $J = 27$, as the limit for the rest of the paper. We remark that although we only show the results for 1σ string stability, similar results can be obtained for $n\sigma$ string stability when $n \neq 1$.

To better understand the above phenomena, we use $\bar{\bar{M}}_0(\omega; J)$, $\bar{\bar{M}}_1(\omega; J)$ and $\bar{\bar{M}}(\omega; J)$ to emphasize their dependence on the number of cars J. Similar to the argument made for the amplification ratio $\bar{M}(\omega; J)$ of the mean dynamics, $\bar{\bar{M}}_1(\omega; J)$ can be approximated by

$$\bar{\bar{M}}_1(\omega; J) \approx \bar{\bar{M}}_1(\omega; 1)^J, \quad \omega > 0, \tag{61}$$

where $\bar{\bar{M}}_1(\omega; 1)^J$ is the amplification ratio of the harmonic fluctuation in the covariance dynamics from the head vehicle to the first vehicle. When $n\sigma$ string stability with $n \geq 1$ is considered, mean string stability condition (37) is the minimum requirement. One can check numerically that

$$\bar{\bar{M}}_1(\omega; J) < 1, \quad \omega > 0, \tag{62}$$

is always satisfied when mean string stability condition holds. Thus, for a fixed $n\sigma$ string stability, as the number of cars J increases, $\bar{M}(\omega;J)$ and $\bar{\bar{M}}_1(\omega;J)$ will both decrease exponentially when mean string stability condition (37) holds, cf. (38) and (61). In other words, the $n\sigma$ string stable condition (60) gets weaker as J increases, resulting in the expansion of $n\sigma$ string stable regions.

However, $\bar{\bar{M}}_0(\omega;J)$ provides a constant excitation to the covariance dynamics (42) and cannot be approximated in the similar way as (38) and (61). Indeed, this constant excitation propagates along the traffic uniformly. To sum up, $\bar{\bar{M}}_0(\omega;J)$ becomes the leading part of (59) when (37) is satisfied and J is sufficiently large. Therefore, we have the following weaker conditions for $n\,\sigma$ string stability.

Definition 2. The system is *$n\sigma$ offset string stable* if the amplitude of the input $\tilde{v}_0(k)$ is attenuated such that

$$\sup_{\omega>0}\bar{M}(\omega)<1,\quad \sup_{\omega>0}\bar{\bar{M}}_0(\omega)<\frac{1}{n^2}. \tag{63}$$

Note that the condition above provides an easier way to check string stability. According to the exponential decaying property in $\bar{M}(\omega;J)$ and $\bar{\bar{M}}_1(\omega;J)$, we have the following proposition.

Proposition 1. *As the number of cars J in the open chain increases, $n\sigma$ string stability and $n\sigma$ offset string stability approximate each other. Moreover, they converge to the same limit as J goes to infinity.*

Fig. 7 summarizes the overall stability diagrams in the (K_v,K_p)-plane for different values of packet delivery ratio p when $J=27$. The same color scheme is used as in Figs. 5 and 6. The mean string stable regions and the 1σ string stable regions are embedded in the corresponding plant stable regions as discussed before. For plant stability, as the packet delivery ratio p decreases, both the mean and covariance plant stable regions shrink, and the differences between them increase. Similar behavior can be observed for the mean string stable and 1σ string stable regions. Fig. 7 also shows us the mean string stability can be used as a good estimate for the 1σ string stability when the open chain is sufficiently long.

4. Closed ring system

In some cases, it may be difficult to use a large open chain system to replicate some traffic phenomena which only appear occasionally. For example, the phantom stop-and-go traffic jams only happen for a string unstable open chain system of large scale when the head vehicle introduces some perturbations. However, this traffic jam will propagate upstream and finally "disappear". Therefore, researchers (Ge et al., 2017; Avedisov and Orosz, 2015) resort to closed ring vehicle system as shown in Fig. 8 that allows to observe such phenomena as sustained oscillations. However, this has only been achieved for deterministic systems in continuous-time domain. In this section, we consider a closed ring system of J connected vehicles with stochastic delays and derive the evolutions for the mean and second moment dynamics in order to evaluate the stability properties.

4.1. Dynamics

Assuming that all the vehicles on the closed ring in Fig. 8 are described by the Eqs. (1) and (5), we can obtain the dynamics for the overall system

$$\begin{aligned}
&\dot{h}_1(t)=v_J(t)-v_1(t),\\
&\dot{v}_1(t)=u_1(t_{k-\tau_1(k)}),\\
&\dot{h}_j(t)=v_{j-1}(t)-v_j(t),\\
&\dot{v}_j(t)=u_j(t_{k-\tau_j(k)}),\quad j=2,\dots,J,
\end{aligned} \tag{64}$$

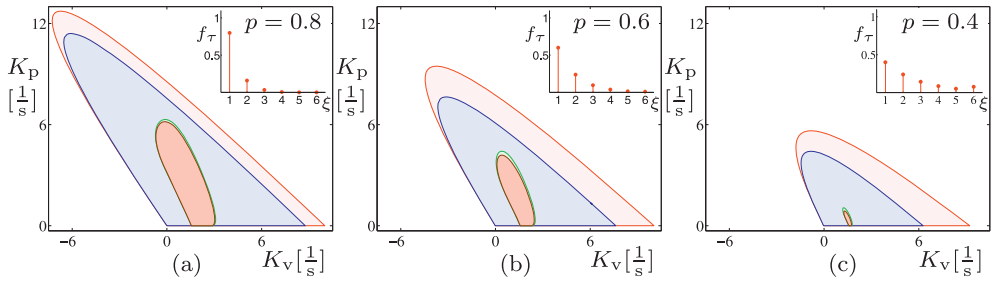

Fig. 7. Stability diagrams for an open chain of $(27+1)$ connected vehicles in the (K_v,K_p)-plane for different values of packet delivery ratio p. Red, blue, green and orange curves represent boundaries for mean plant stability, second moment plant stability, mean string stability and 1σ string stability, respectively, while the light red, light blue, light green and light orange shaded regions represent the corresponding stability regions.

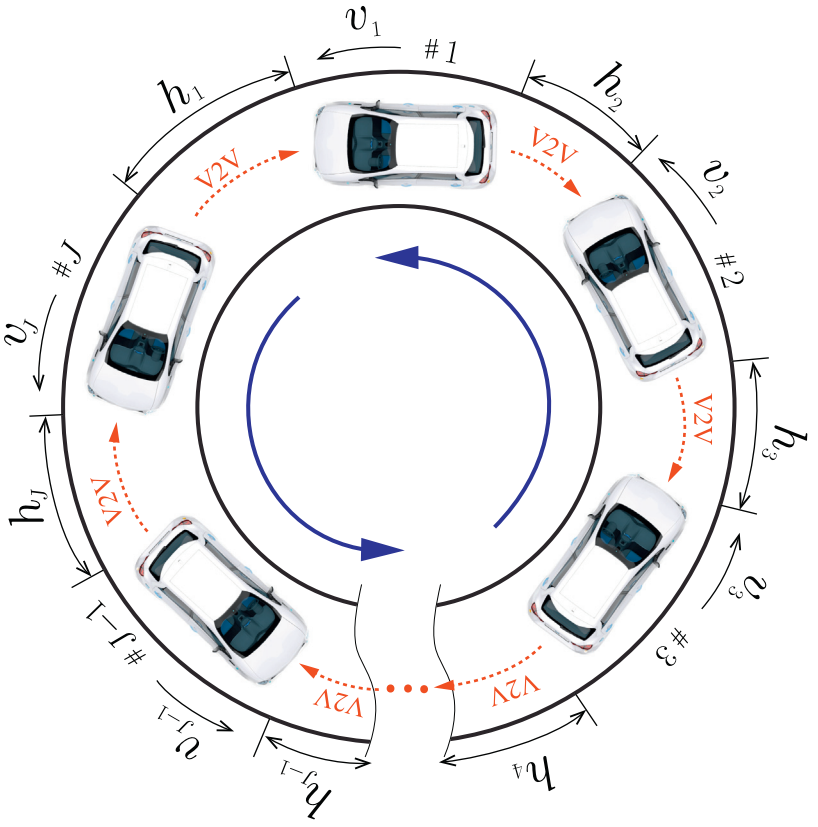

Fig. 8. A closed ring of J connected vehicles on a single lane. Dashed red arrows indicate the information flow through wireless communication, while the solid blue arrows indicate the direction of traffic flow.

for $t_k \le t < t_{k+1}$. Using the fact that $u_j(t_{k-\tau_j})$ is a constant in the time interval $t \in [t_k, t_{k+1})$, one can solve the differential Eq. (64) directly with initial values $h(t_k), v(t_k)$, yielding the discrete-time nonlinear map

$$\begin{aligned}
h_1(t_{k+1}) &= h_1(t_k) + \big(v_J(t_k) - v_1(t_k)\big)\Delta t + \frac{1}{2}\Big(u_J(t_{k-\tau_J}) - u_1(t_{k-\tau_1})\Big)\Delta t^2,\\
v_1(t_{k+1}) &= v_1(t_k) + u_1(t_{k-\tau_1})\Delta t,\\
h_j(t_{k+1}) &= h_j(t_k) + \big(v_{j-1}(t_k) - v_j(t_k)\big)\Delta t + \frac{1}{2}\Big(u_{j-1}(t_{k-\tau_{j-1}}) - u_j(t_{k-\tau_j})\Big)\Delta t^2,\\
v_j(t_{k+1}) &= v_j(t_k) + u_j(t_{k-\tau_j})\Delta t, \quad j = 2, \ldots, J.
\end{aligned} \tag{65}$$

The uniform flow equilibrium is achieved when all the vehicles reach the same velocity and distance headway given in (8). Recall that in the open chain, the head vehicle determines the equilibrium velocity and (8) was used to devise the equilibrium distance headway; while in the closed ring, the length of the road and the number of cars determine the equilibrium distance headway and (8) is used to obtain the equilibrium velocity.

Following the same process as we discussed in the case of open chain, we can define perturbations, states and augmented states as (10), (12), (17), and (19), and obtain the stochastic dynamics

$$X(k+1) = \mathbf{A}^{\mathrm{R}}_{\boldsymbol{\tau}} X(k), \tag{66}$$

where the possible values for $\mathbf{A}^{\mathrm{R}}_{\boldsymbol{\tau}}$ are given in (C.1) in Appendix C.

With the IID assumption for the delays and the definition of the deterministic variables $\bar{X}(k)$ in (22), one can derive the equation for the mean dynamics

$$\bar{X}(k+1) = \bar{\mathbf{A}}^{\mathrm{R}} \bar{X}(k), \tag{67}$$

by taking expectations of both sides in (66), where

$$\bar{\mathbf{A}}^{\mathrm{R}} = \sum_{r=1}^{N} w_r \mathbf{A}^{\mathrm{R}}_{\boldsymbol{r}}, \tag{68}$$

and the explicit expression of $\bar{\mathbf{A}}^{\mathrm{R}}$ is given in (C.2) in Appendix C.

Similarly, using the definition of the variable $\hat{\hat{X}}(k)$ in (25), one can obtain the second moment dynamics

$$\hat{\hat{X}}(k+1) = \bar{\bar{\mathbf{A}}}^{\mathrm{R}} \hat{\hat{X}}(k), \tag{69}$$

by taking expectations with the PDF-s (21) and using independency between variables, where

$$\bar{\bar{\mathbf{A}}}^{\mathrm{R}} = \sum_{r=1}^{N} w_r \mathbf{A}_r^{\mathrm{R}} \otimes \mathbf{A}_r^{\mathrm{R}}. \tag{70}$$

We remark that the covariance dynamics can also be obtained for the closed ring system. However, it is not needed for stability analysis.

4.2. Stability

Unlike open chain systems, the closed ring system does not have the definition of string stability due to the lack of input, cf. (64)–(66), and plant stability reduces to the normal definition of stability in control theory. However, (Ge et al., 2017) unveils the relationship between the stability of the closed ring system and the string stability of the open chain system with the same configuration in the deterministic case in continuous-time domain. In this section, we investigate the stability of the mean dynamics (67) and the second moment dynamics (69) of the closed ring system shown in Fig. 8, following the method discussed in the case of open chain systems, in order to find the relationship between two different systems in the stochastic sense in discrete-time domain.

To demonstrate stability, Fig. 9 shows three simulation results for a closed ring of 55 vehicles for different $(K_{\mathrm{v}}, K_{\mathrm{p}})$ gains when the packet delivery ratio $p = 0.4$. The other parameters used here remain the same as those for Fig. 3. Again only the velocities of every 11-th vehicles are shown. Fig. 9(a) shows a case when the equilibrium is stable. It can be seen that all the vehicles' velocities approach the desired equilibrium velocity despite the initial perturbations and stochastic packet drops. In this sense, this realization for the stochastic closed ring system is stable. However, similar to the argument for the open chain system, to check whether this pair of $(K_{\mathrm{v}}, K_{\mathrm{p}})$ gains is stable in the stochastic sense, one has to investigate all the possible realizations. Fig. 9(b, c) shows two different scenarios when the equilibrium is unstable. In Fig. 9(b), the vehicles are unable to settle down to the desired velocity and keep oscillating around it due to the stochastic packet drops. This oscillation in traffic system will deteriorate fuel economy and driving comfort. However, a more severe situation happens in Fig. 9(c), where the initial perturbation causes stop-and-go traffic jams. The goal of the controller design is to eliminate all these unstable behaviors by ensuring stability of the uniform flow equilibrium.

For stability of the mean dynamics (67), all the eigenvalues of the matrix $\bar{\mathbf{A}}^{\mathrm{R}}$ must lie within the unit circle in the complex plane. Notice that $\bar{\mathbf{A}}^{\mathrm{R}}$ (cf. (C.2)) is a banded block circulant matrix (Davis, 1979; Olson et al., 2014), so the real matrix $\bar{\mathbf{A}}^{\mathrm{R}}$ is unitarily similar to a block diagonal matrix with diagonal blocks

$$\bar{\mathbf{\Lambda}}_i = \bar{\boldsymbol{\alpha}}_1 + \bar{\boldsymbol{\alpha}}_4 \mathrm{e}^{-\mathrm{j}\frac{2\pi}{J}2(i-1)} + (\bar{\boldsymbol{\alpha}}_2 + \bar{\boldsymbol{\alpha}}_3)\mathrm{e}^{-\mathrm{j}\frac{2\pi}{J}(i-1)}, \quad 1 \leqslant i \leqslant J, \tag{71}$$

cf. (A.4). This can be obtained by using a transformation matrix that is the Kronecker product of the J-dimensional Fourier matrix and the $2(N+1)$-dimensional identity matrix. In order to assure the mean stability, the eigenvalues of the matrices $\bar{\mathbf{\Lambda}}_i$, $1 \leq i \leq J$, must lie within the unit circle in the complex plane. Notice that $\bar{\mathbf{A}}^{\mathrm{R}}$ is of dimension $2J(N+1)$, but $\bar{\mathbf{\Lambda}}_i$ is of dimension $2(N+1)$. Also,

$$\mathrm{e}^{\mathrm{j}\frac{2\pi}{J}(i-1)}, \quad 1 \leqslant i \leqslant J, \tag{72}$$

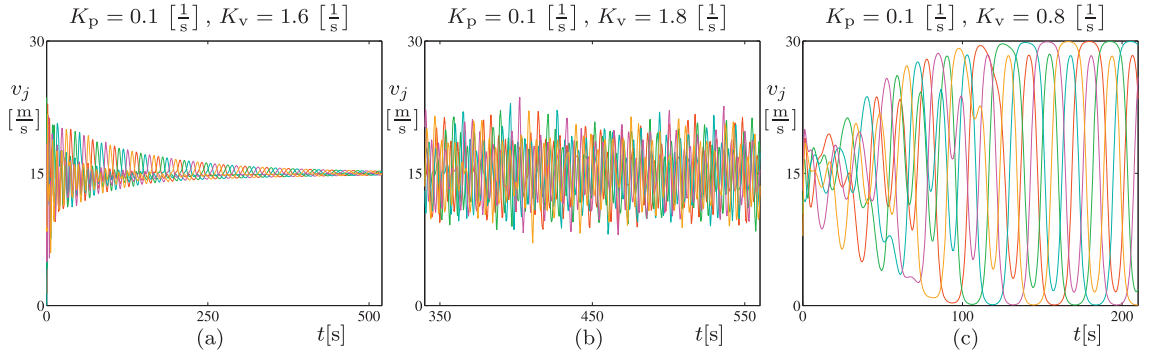

Fig. 9. Simulations of a closed ring of 55 connected vehicles for different $(K_{\mathrm{v}}, K_{\mathrm{p}})$ gains as indicated. The red, green, cyan, magenta and orange curves represent the velocities v_{11}, v_{22}, v_{33}, v_{44}, v_{55}, respectively. (a) Stable. (b) Unstable. (c) Unstable.

is the collection of all the J-th roots of unity. For $J \to \infty, \theta$ can take all the possible values on the unit circle in the complex plane. Thus, (71) yields the stability condition for the mean dynamics of the closed ring of infinitely many vehicles, that is, all the eigenvalues of the matrix

$$\bar{\mathbf{\Lambda}}_\theta = \bar{\boldsymbol{\alpha}}_1 + \bar{\boldsymbol{\alpha}}_4 \mathrm{e}^{-2\mathrm{j}\theta} + (\bar{\boldsymbol{\alpha}}_2 + \bar{\boldsymbol{\alpha}}_3)\mathrm{e}^{-\mathrm{j}\theta}, \tag{73}$$

lie within the unit circle in the complex plane for any $0 \le \theta \le \pi$. Here, the fact that the eigenvalues of a real matrix appear as conjugate pairs are used. We also remark that the limit $J \to \infty$ is taken such that the length of the ring is also increased to infinity while h^* is kept constant.

Fig. 10 shows the mean stability diagrams of the closed ring system in the $(K_\mathrm{v}, K_\mathrm{p})$-plane for different values of packet delivery ratio p and numbers of vehicles J. The solid cyan lines and curves correspond to mean stability boundaries for the closed ring of $J = 3, 9, 15, 21, 27$ vehicles such that the darker the color is, the more vehicles there are. The regions enclosed by these curves are the mean stable regions. As the number of vehicles J increases, the mean stable regions converge to the corresponding mean stable regions of the closed ring system of infinitely many vehicles. The limit mean stable boundaries are represented by the dashed cyan lines and curves, and the corresponding mean stable regions are shown as light cyan shaded regions. We remark that as the number of vehicles in the closed ring increases, the mean stable regions shrink, but the mean stable conditions for a closed ring of J_1 cars is neither a necessary nor a sufficient condition for that of J_2 cars when $J_1 \le J_2$.

Similarly, to ensure stability of the second moment dynamics (69) for the closed ring system, all the eigenvalues of the matrix $\bar{\bar{\mathbf{A}}}^\mathrm{R}$ must lie within the unit circle in the complex plane. Again we are faced with same issues as in the case of the open chain, i.e., an enormous enumeration of high dimensional matrices $\mathbf{A}_\mathbf{r}^\mathrm{R} \otimes \mathbf{A}_\mathbf{r}^\mathrm{R}$ while constructing $\bar{\bar{\mathbf{A}}}^\mathrm{R}$, as well as frequent eigenvalue calculations for this high dimensional matrix while varying parameters. As laid out in the supplemental document, by applying properties of Kronecker product and using perfect shuffles, matrix $\bar{\bar{\mathbf{A}}}^\mathrm{R}$ can be transformed into a block circulant matrix $\hat{\bar{\bar{\mathbf{A}}}}^\mathrm{R}$, and only N weighted sum of lower dimensional matrices is needed. This block circulant real matrix $\hat{\bar{\bar{\mathbf{A}}}}^\mathrm{R}$ is unitarily similar to a block diagonal complex matrix with diagonal blocks

$$\bar{\bar{\mathbf{\Lambda}}}_i \in \mathbb{R}^{2^2 J(N+1)^2 \times 2^2 J(N+1)^2}, \quad 1 \leqslant i \leqslant J, \tag{74}$$

which are not shown here explicitly due to the complexity, but can be found in the supplemental document. Thus, in order to assure the second moment stability of the closed ring, we need to make sure that all the eigenvalues of the matrices $\bar{\bar{\mathbf{\Lambda}}}_i$, $1 \le i \le J$, lie within the unit circle in the complex plane. Here, we remark that $\bar{\bar{\mathbf{\Lambda}}}_i$ is a perturbed block penta-circulant matrix, but the perturbed block elements caused by vehicular connectivity prevent us from further simplifications. If one can succeed in reducing this eigenvalue problem of $\bar{\bar{\mathbf{\Lambda}}}_i$ to the eigenvalue problem of matrices of even lower dimension, possibly $2^2(N+1)^2$, then for the closed ring system of infinitely many vehicles, the stability condition for the second moment dynamics can be obtained in the same way as that for the mean dynamics, cf. (73).

Fig. 11 shows the stability diagrams of the second moment dynamics in the $(K_\mathrm{v}, K_\mathrm{p})$-plane for different values of packet delivery ratio p and numbers of cars J. The purple lines and curves correspond to the second moment stability boundaries for the closed ring of $J = 3, 9, 15, 21, 27$ vehicles in the way that the darker the purple color is, the more vehicles there are. Similar to the mean dynamics, as the number of vehicles J increases, the second moment stable region converges to a limit, that is given by the case of infinitely many vehicles. However, this limit is hard to obtain due to the aforementioned perturbed terms in $\bar{\bar{\mathbf{\Lambda}}}_i$. Therefore, we take the results for the largest number of vehicles J we can calculate so far, i.e., $J = 27$, as the limit, and shade the corresponding second moment stable regions with light purple color in Fig. 11. Again we remark that as the number of vehicles increases, the second moment stable regions shrink in a similar way as the mean stable regions do.

In order to highlight the difference between mean stability and second moment stability, Fig. 12 shows the overall stability diagrams in the $(K_\mathrm{v}, K_\mathrm{p})$-plane for different values of packet delivery ratio p when $J = 27$. The same color scheme is

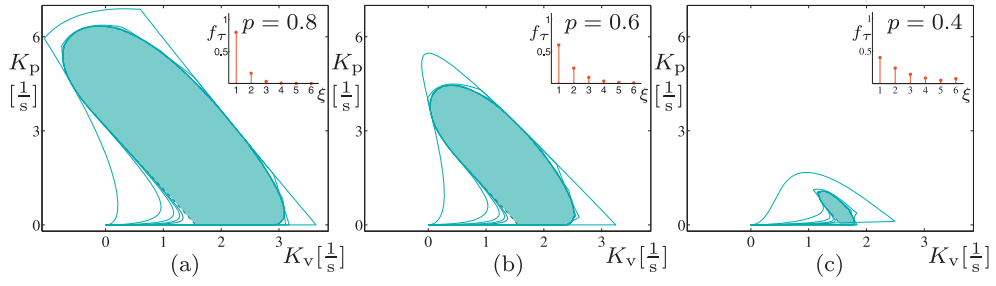

Fig. 10. Mean stability diagrams for a closed ring of J connected vehicles in the $(K_\mathrm{v}, K_\mathrm{p})$-plane for different values of packet delivery ratio p. The cyan lines and curves represent stability boundaries. Each panel plots all the boundaries corresponding to $J = 3, 9, 15, 21, 27$ from light cyan to dark cyan curves, while the dashed cyan curves correspond to the case $J \to \infty$.

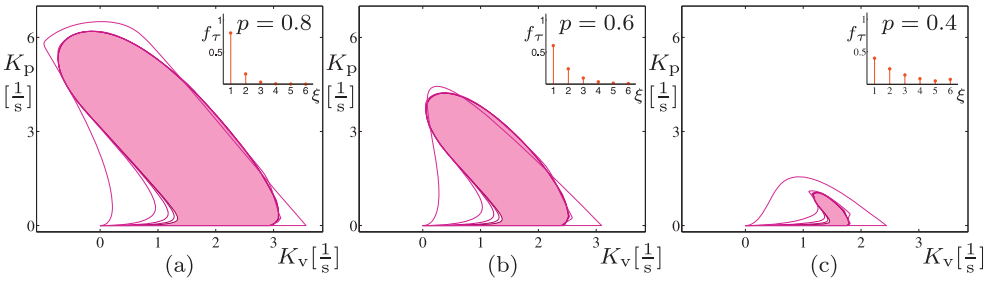

Fig. 11. Second moment stability diagrams for a closed ring of J connected vehicles in the (K_v, K_p)-plane for different values of packet delivery ratio p. Each panel plots all the boundaries corresponding to $J = 3, 9, 15, 21, 27$ from light purple to dark purple curves.

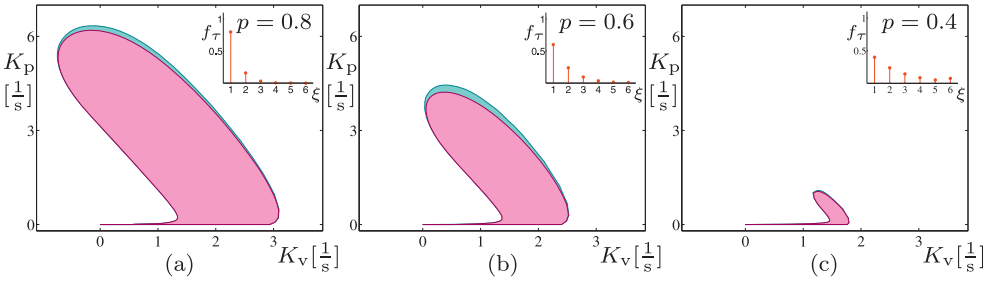

Fig. 12. Mean and second moment stability diagrams for a closed ring of 27 connected vehicles in the (K_v, K_p)-plane for different values of packet delivery ratio p. Cyan curves and purple curves represent the boundaries for mean stability and second moment stability, respectively, while the light cyan and light purple shaded regions represent the mean stable regions and second moment stable regions, respectively.

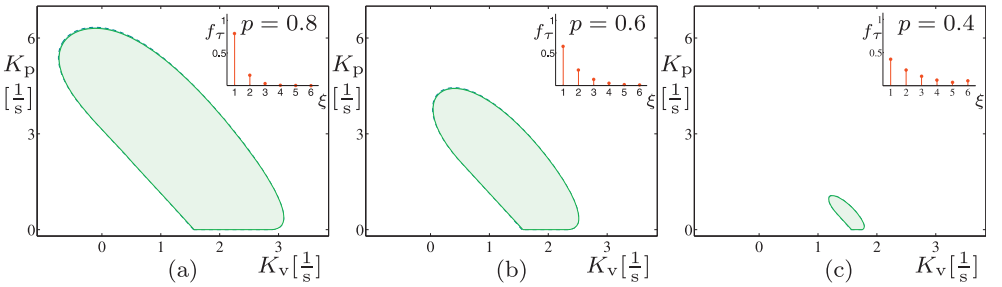

Fig. 13. Comparison diagrams between mean string stability of an open chain and mean stability of a closed ring in the (K_v, K_p)-plane for different values of packet delivery ratio p. The solid green curves represent mean string stability boundaries for an open chain of $(3 + 1)$ vehicles, while the dashed cyan curves represent mean stability boundaries for a closed ring of infinitely many vehicles.

used as in Figs. 10 and 11. The second moment stable regions are embedded in the corresponding mean stable regions as discussed before. As the packet delivery ratio p decreases, both the mean and second moment stable regions shrink. Fig. 12 demonstrates that the mean stability can be used as a good estimate for the second moment stability of the closed ring system when the packet delivery ratio p is sufficiently large.

5. Comparison of results

In this section, we compare the stability results of the open chain system in Fig. 2 and closed ring system in Fig. 8 in the presence of stochastic delays due to packet drops, where all the vehicles are described by the Eqs. (1) and (5).

Fig. 13 shows the comparison diagrams between the mean string stability for the open chain system of $(3 + 1)$ vehicles and the mean stability for the closed ring system of infinitely many vehicles in the (K_v, K_p)-plane for different values of packet delivery ratio p. The same color scheme is used as in Figs. 6 and 10. We recall that the mean string stability for the open chain system has an extremely weak dependence on the number of vehicles in the system, so mean string stability for the open chain system of $(3 + 1)$ vehicles can be used as a good estimate for the open chain system of infinitely many vehicles. It can be seen that the mean string stability for the open chain and mean stability for the closed ring for the same

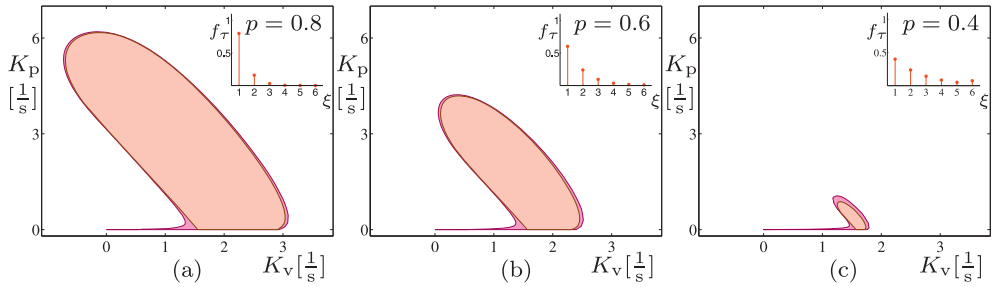

Fig. 14. Comparison diagrams between 1σ string stability of an open chain, and second moment stability of a closed ring in the (K_v, K_p)-plane for different values of packet delivery ratio p. The solid orange curves and light orange shaded regions represent 1σ string stability boundaries and 1σ string stable regions for an open chain of $(27 + 1)$ vehicles, while the solid purple curves and light purple shaded regions represent second moment stability boundaries and second moment stable regions for a closed ring of 27 vehicles, respectively.

parameter are practically indistinguishable. In other words, the mean string stability for the open chain system and mean stability for the closed ring system with the same configuration converge to the same limit as the number of vehicles in the system goes to infinity.

Fig. 14 shows the comparison between the 1σ string stability for the open chain system of $(27 + 1)$ vehicles and the second moment stability for the closed ring system of 27 vehicles in the (K_v, K_p)-plane for different values of packet delivery ratio p. The same color scheme is used as in Figs. 6 and 11. It can be seen that the difference between the 1σ string stability for the open chain system and second moment stability for the closed ring system for the same parameters is rather small except that the second moment stable regions for the closed ring system have extra "peninsulas" that indeed disappear as the number of vehicles J goes to infinity (similar to the mean stable regions). Therefore, the 1σ string stability for the open chain system and second moment stability for the closed ring system are essentially the same for large numbers of vehicles.

6. Conclusions

In this paper, we analyzed the dynamics of large connected vehicle systems using open chain and closed ring configurations. We showed that packet drops lead to stochastic delay variations and we derived the mean, second moment, and covariance dynamics in order to characterize the dynamics in the vicinity of the uniform flow. We established novel decomposition techniques that allowed us to significantly reduce the size of the eigenvalue problems when analyzing stability.

For the open chain system, plant stability and $n\sigma$ string stability results were illustrated using stability diagrams on the plane of gain parameters while varying the packet delivery ratio and the number of vehicles. It was found that both the mean and the second moment plant stability are independent of the number of vehicles in the system. The mean string stability has a very week dependence on the number of vehicles while the 1σ string stable region expands as the number of vehicles increases. Our results demonstrated that for large numbers of vehicles and sufficiently large packet delivery ratio the mean string stability can be used as a good estimate for the 1σ string stability.

For the closed ring system, stability charts were drawn using the mean and the second moment dynamics. We illustrated that the stable regions shrink and converge to some limits as the number of vehicles increases. These limits can be obtained by analyzing the case of infinitely many vehicles on the ring. Again the mean stability is a good estimate for the second moment stability when the number of vehicles and packet delivery ratio are large enough. We also found that the mean string stable region of open chain and mean stable region of the closed ring converge to the same limit as the number of vehicles goes to infinity. Similarly, the 1σ string stable region of the open chain and second moment stability of the closed ring converge to the same limit.

Our results illustrate the feasibility of using connected vehicles to change the large scale dynamics of transportation systems in the presence of packet drops and provide the necessary mathematical tools in order to design connectivity-based controllers that can ensure smooth traffic flow.

Acknowledgment

This work was supported by NSF grant 1300319.

Appendix A. Common matrices used for both systems

The matrices in (14) are given by

$$\boldsymbol{a}_1 = \begin{bmatrix} 1 & -\Delta t \\ 0 & 1 \end{bmatrix}, \quad \boldsymbol{a}_2 = \begin{bmatrix} 0 & \Delta t \\ 0 & 0 \end{bmatrix}, \quad \boldsymbol{a}_3 = \begin{bmatrix} -\frac{1}{2}\Delta t^2 K_\mathrm{p} N_* & \frac{1}{2}\Delta t^2 (K_\mathrm{p} + K_\mathrm{v}) \\ \Delta t K_\mathrm{p} N_* & -\Delta t (K_\mathrm{p} + K_\mathrm{v}) \end{bmatrix},$$
$$\boldsymbol{a}_4 = \begin{bmatrix} 0 & -\frac{1}{2}\Delta t^2 K_\mathrm{v} \\ 0 & \Delta t K_\mathrm{v} \end{bmatrix}, \quad \boldsymbol{a}_5 = \begin{bmatrix} \frac{1}{2}\Delta t^2 K_\mathrm{p} N_* & -\frac{1}{2}\Delta t^2 (K_\mathrm{p} + K_\mathrm{v}) \\ 0 & 0 \end{bmatrix}, \quad \boldsymbol{a}_6 = \begin{bmatrix} 0 & \frac{1}{2}\Delta t^2 K_\mathrm{v} \\ 0 & 0 \end{bmatrix},$$
$$\boldsymbol{b}_1 = \begin{bmatrix} \frac{\sin(\omega \Delta t)}{\omega} & \frac{1-\cos(\omega \Delta t)}{\omega} \\ 0 & 0 \end{bmatrix}, \quad \boldsymbol{b}_2 = \begin{bmatrix} -\frac{1}{2}\Delta t^2 K_\mathrm{v} & 0 \\ \Delta t K_\mathrm{v} & 0 \end{bmatrix}, \quad \boldsymbol{b}_3 = \begin{bmatrix} \frac{1}{2}\Delta t^2 K_\mathrm{v} & 0 \\ 0 & 0 \end{bmatrix}, \tag{A.1}$$

$$c_1 = [0 \quad 1].$$

where

$$N_* = \frac{\mathrm{d}V(h_j^*)}{\mathrm{d}h} = \begin{cases} \frac{\pi \sqrt{v_j^*(v_\mathrm{max} - v_j^*)}}{h_\mathrm{go} - h_\mathrm{st}} & \text{if } h_\mathrm{st} < h_j < h_\mathrm{go}, \\ 0 & \text{elsewhere}, \end{cases} \tag{A.2}$$

cf. (6).

In (18), $\boldsymbol{\alpha}_{1,\tau_j}, \boldsymbol{\alpha}_{2,\tau_j}, \boldsymbol{\alpha}_{3,\tau_j}, \boldsymbol{\alpha}_{4,\tau_j} \in \mathbb{R}^{2(N+1)\times 2(N+1)}$ and $\boldsymbol{\beta}_{1,\tau_1}, \boldsymbol{\beta}_{2,\tau_1} \in \mathbb{R}^{2(N+1)\times 2}$ can take the values

$$\boldsymbol{\alpha}_{1,r_j} = \begin{bmatrix} \boldsymbol{a}_1 & \delta_{1r_j}\boldsymbol{a}_3 & \dots & \delta_{Nr_j}\boldsymbol{a}_3 \\ \mathbf{I} & & & \\ & \ddots & & \\ & & & \mathbf{I} \end{bmatrix}, \quad \boldsymbol{\alpha}_{2,r_j} = \begin{bmatrix} \boldsymbol{a}_2 & \delta_{1r_j}\boldsymbol{a}_4 & \dots & \delta_{Nr_j}\boldsymbol{a}_4 \\ \mathbf{0} & \mathbf{0} & \dots & \mathbf{0} \end{bmatrix},$$
$$\boldsymbol{\alpha}_{3,r_j} = \begin{bmatrix} \mathbf{0} & \delta_{1r_j}\boldsymbol{a}_5 & \dots & \delta_{Nr_j}\boldsymbol{a}_5 \\ \mathbf{0} & \mathbf{0} & \dots & \mathbf{0} \end{bmatrix}, \quad \boldsymbol{\alpha}_{4,r_j} = \begin{bmatrix} \mathbf{0} & \delta_{1r_j}\boldsymbol{a}_6 & \dots & \delta_{Nr_j}\boldsymbol{a}_6 \\ \mathbf{0} & \mathbf{0} & \dots & \mathbf{0} \end{bmatrix}, \tag{A.3}$$
$$\boldsymbol{\beta}_{1,r_1} = \begin{bmatrix} \boldsymbol{b}_1 + \sum_{n=1}^{N} \delta_{nr_1} \boldsymbol{b}_2 \mathbf{R}^n \\ \mathbf{0} \\ \vdots \\ \mathbf{0} \end{bmatrix}, \boldsymbol{\beta}_{2,r_1} = \begin{bmatrix} \sum_{n=1}^{N} \delta_{nr_1} \boldsymbol{b}_3 \mathbf{R}^n \\ \mathbf{0} \\ \vdots \\ \mathbf{0} \end{bmatrix},$$

for $r_j = 1, 2, \cdots, N$, where δ_{ir_j} denotes the Kronecker delta, and $j = 1, 2, \dots, J$. The expected values of $\boldsymbol{\alpha}_{1,\tau_j}, \boldsymbol{\alpha}_{2,\tau_j}, \boldsymbol{\alpha}_{3,\tau_j}, \boldsymbol{\alpha}_{4,\tau_j}, \boldsymbol{\beta}_{1,\tau_1}, \boldsymbol{\beta}_{2,\tau_1}$ are

$$\bar{\boldsymbol{\alpha}}_1 = \sum_{r_j=1}^{N} w_{r_j} \boldsymbol{\alpha}_{1,r_j} = \begin{bmatrix} \boldsymbol{a}_1 & w_1\boldsymbol{a}_3 & \dots & w_N\boldsymbol{a}_3 \\ \mathbf{I} & & & \\ & \ddots & & \\ & & & \mathbf{I} \end{bmatrix}, \quad \bar{\boldsymbol{\alpha}}_2 = \sum_{r_j=1}^{N} w_{r_j} \boldsymbol{\alpha}_{2,r_j} = \begin{bmatrix} \boldsymbol{a}_2 & w_1\boldsymbol{a}_4 & \dots & w_N\boldsymbol{a}_4 \\ \mathbf{0} & \mathbf{0} & \dots & \mathbf{0} \end{bmatrix},$$
$$\bar{\boldsymbol{\alpha}}_3 = \sum_{r_j=1}^{N} w_{r_j} \boldsymbol{\alpha}_{3,r_j} = \begin{bmatrix} \mathbf{0} & w_1\boldsymbol{a}_5 & \dots & w_N\boldsymbol{a}_5 \\ \mathbf{0} & \mathbf{0} & \dots & \mathbf{0} \end{bmatrix}, \quad \bar{\boldsymbol{\alpha}}_4 = \sum_{r_j=1}^{N} w_{r_j} \boldsymbol{\alpha}_{4,r_j} = \begin{bmatrix} \mathbf{0} & w_1\boldsymbol{a}_6 & \dots & w_N\boldsymbol{a}_6 \\ \mathbf{0} & \mathbf{0} & \dots & \mathbf{0} \end{bmatrix},$$
$$\bar{\boldsymbol{\beta}}_1 = \sum_{r_j=1}^{N} w_{r_j} \boldsymbol{\beta}_{1,r_j} = \begin{bmatrix} \boldsymbol{b}_1 + \boldsymbol{b}_2\bar{\mathbf{R}} \\ \mathbf{0} \\ \vdots \\ \mathbf{0} \end{bmatrix}, \quad \bar{\boldsymbol{\beta}}_2 = \sum_{r_j=1}^{N} w_{r_j} \boldsymbol{\beta}_{2,r_j} = \begin{bmatrix} \boldsymbol{b}_3\bar{\mathbf{R}} \\ \mathbf{0} \\ \vdots \\ \mathbf{0} \end{bmatrix}, \tag{A.4}$$

where

$$\bar{\mathbf{R}} = \sum_{n=1}^{N} w_n \mathbf{R}^n. \tag{A.5}$$

Appendix B. Matrices used for open chain

The output matrix in (18) is

$$\boldsymbol{c} = \begin{bmatrix} c_1 & 0' & \dots & 0' \end{bmatrix}, \tag{B.1}$$

where

$$0\prime = [0 \quad 0], \tag{B.2}$$

and the output matrix in (20) is

$$\mathbf{C} = [\mathbf{0} \quad \dots \quad \mathbf{0} \quad \boldsymbol{c}], \tag{B.3}$$

where $\mathbf{0}$ is a $2(N+1)$-dimensional row vector with all elements being 0.

In (20), $\mathbf{A}_\tau$ and $\mathbf{B}_{\tau_1}$ can take the values from

$$\mathbf{A}_{\boldsymbol{r}} = \begin{bmatrix} \boldsymbol{\alpha}_{1,r_1} & & & & & \\ \boldsymbol{\alpha}_{3,r_1}+\boldsymbol{\alpha}_{2,r_2} & \boldsymbol{\alpha}_{1,r_2} & & & & \\ \boldsymbol{\alpha}_{4,r_2} & \boldsymbol{\alpha}_{3,r_2}+\boldsymbol{\alpha}_{2,r_3} & \boldsymbol{\alpha}_{1,r_3} & & & \\ & \ddots & \ddots & \ddots & & \\ & & \boldsymbol{\alpha}_{4,r_{j-1}} & \boldsymbol{\alpha}_{3,r_{j-1}}+\boldsymbol{\alpha}_{2,r_j} & \boldsymbol{\alpha}_{1,r_j} \end{bmatrix}, \quad \mathbf{B}_{r_1} = \begin{bmatrix} \boldsymbol{\beta}_{1,r_1} \\ \boldsymbol{\beta}_{2,r_1} \\ \mathbf{0} \\ \vdots \\ \mathbf{0} \end{bmatrix}, \tag{B.4}$$

for $r_j = 1, 2, \cdots, N$, and $j = 1, 2, \dots, J$, cf. (A.3).

The explicit expression for those matrices in (23) are given by

$$\bar{\mathbf{A}} = \begin{bmatrix} \bar{\boldsymbol{\alpha}}_1 & & & & \\ \bar{\boldsymbol{\alpha}}_3+\bar{\boldsymbol{\alpha}}_2 & \bar{\boldsymbol{\alpha}}_1 & & & \\ \bar{\boldsymbol{\alpha}}_4 & \bar{\boldsymbol{\alpha}}_3+\bar{\boldsymbol{\alpha}}_2 & \bar{\boldsymbol{\alpha}}_1 & & \\ & \ddots & \ddots & \ddots & \\ & & \bar{\boldsymbol{\alpha}}_4 & \bar{\boldsymbol{\alpha}}_3+\bar{\boldsymbol{\alpha}}_2 & \bar{\boldsymbol{\alpha}}_1 \end{bmatrix}, \quad \bar{\mathbf{B}} = \begin{bmatrix} \bar{\boldsymbol{\beta}}_1 \\ \bar{\boldsymbol{\beta}}_2 \\ \mathbf{0} \\ \vdots \\ \mathbf{0} \end{bmatrix}, \tag{B.5}$$

cf. (A.4).

We remark that if a different connectivity topology is used, some changes occur in (B.4) and (B.5) while the proposed decomposition method still works. For example, if vehicles use the information of multiple predecessors instead of just the immediate predecessor (Zhang and Orosz, 2016; Li et al., 2015), non-zero block elements appear under the second sub-diagonal of block matrices $\mathbf{A}_{\boldsymbol{r}}$ and $\bar{\mathbf{A}}$, and $\mathbf{B}_{r_1}$ and $\bar{\mathbf{B}}$ also change accordingly. Also, if vehicles have heterogeneous controllers, difference in block elements will show the corresponding heterogeneity.

Appendix C. Matrices used for closed ring

In (66), $\mathbf{A}^{\mathrm{R}}_\tau$ can take the values from

$$\mathbf{A}^{\mathrm{R}}_{\boldsymbol{r}} = \begin{bmatrix} \boldsymbol{\alpha}_{1,r_1} & & & & \boldsymbol{\alpha}_{4,r_J} & \boldsymbol{\alpha}_{3,r_J}+\boldsymbol{\alpha}_{2,r_1} \\ \boldsymbol{\alpha}_{3,r_1}+\boldsymbol{\alpha}_{2,r_2} & \boldsymbol{\alpha}_{1,r_2} & & & & \boldsymbol{\alpha}_{4,r_1} \\ \boldsymbol{\alpha}_{4,r_2} & \boldsymbol{\alpha}_{3,r_2}+\boldsymbol{\alpha}_{2,r_3} & \boldsymbol{\alpha}_{1,r_3} & & & \\ & \ddots & \ddots & \ddots & & \\ & & \boldsymbol{\alpha}_{4,r_{j-1}} & \boldsymbol{\alpha}_{3,r_{j-1}}+\boldsymbol{\alpha}_{2,r_j} & & \boldsymbol{\alpha}_{1,r_j} \end{bmatrix}, \tag{C.1}$$

for $r_j = 1, 2, \cdots, N$, and $j = 1, 2, \dots, J$, cf. (A.3).

In (67), the explicit expression for matrix $\bar{\mathbf{A}}^{\mathrm{R}}$ is

$$\bar{\mathbf{A}}^{\mathrm{R}} = \sum_{\boldsymbol{r}=1}^{N} w_{\boldsymbol{r}} \mathbf{A}^{\mathrm{R}}_{\boldsymbol{r}} = \begin{bmatrix} \bar{\boldsymbol{\alpha}}_1 & & & & \bar{\boldsymbol{\alpha}}_4 & \bar{\boldsymbol{\alpha}}_3+\bar{\boldsymbol{\alpha}}_2 \\ \bar{\boldsymbol{\alpha}}_3+\bar{\boldsymbol{\alpha}}_2 & \bar{\boldsymbol{\alpha}}_1 & & & & \bar{\boldsymbol{\alpha}}_4 \\ \bar{\boldsymbol{\alpha}}_4 & \bar{\boldsymbol{\alpha}}_3+\bar{\boldsymbol{\alpha}}_2 & \bar{\boldsymbol{\alpha}}_1 & & & \\ & \ddots & \ddots & \ddots & & \\ & & \bar{\boldsymbol{\alpha}}_4 & \bar{\boldsymbol{\alpha}}_3+\bar{\boldsymbol{\alpha}}_2 & & \bar{\boldsymbol{\alpha}}_1 \end{bmatrix}, \tag{C.2}$$

cf. (A.4).

Here we remark again that different connectivity topology or heterogeneous controllers will change the above matrices. However, while the proposed decomposition method still work for different connectivity topology, it has some limitations when heterogeneous controllers are considered, since heterogeneity breaks the block circulant structure of matrix $\bar{\mathbf{A}}^{\mathrm{R}}$. In this case, no further simplification can be achieved.

Using different connectivity topology or heterogeneous controllers will change the above matrices. The proposed decomposition method still works for different connectivity topology. For heterogeneous controllers the block circulant structure of matrix $\bar{\mathbf{A}}^{\mathrm{R}}$ disappears that may prohibit further simplifications.

Appendix D. Almost sure stability

Definition 3. A random sequence $\{X(k) \in \mathbb{R}^n\}_{k=0}^{+\infty}$ converges to X^* almost surely if

$$\mathbb{P}\left[\lim_{k\to\infty} X(k) = X^*\right] = 1. \tag{D.1}$$

If sequences generated by a stochastic dynamical system converge to X^* almost surely, then the solution $X(k) \equiv X^*$ is almost surely asymptotically stable.

Appendix E. Supplementary material

Supplementary data associated with this article can be found, in the online version, at http://dx.doi.org/10.1016/j.trc.2017.07.005.

References

Avedisov, S.S., Orosz, G., 2015. Nonlinear network modes in cyclic systems with applications to connected vehicles. J. Nonlinear Sci. 25 (4), 1015–1049.
Bachrathy, D., Stépán, G., 2012. Bisection method in higher dimensions and the efficiency number. Periodica Polytechnica 56 (2), 81–86.
Chan, E., Gilhead, P., Jelínek, P., Krejčí, P., Robin, T., 2012. Cooperative control of SARTRE automated platoon vehicles. In: 19th ITS World Congress. ITS, Vienna, Austria.
Davio, M., 1981. Kronecker products and shuffle algebra. IEEE Trans. Comput. C-30 (2), 116–125.
Davis, L.C., 2007. Effect of adaptive cruise control systems on mixed traffic flow near an on-ramp. Physica A 379 (1), 274–290.
Davis, P.J., 1979. Circulant Matrices. John Wiley & Sons, Inc..
Desjardins, C., Chaib-draa, B., 2011. Cooperative adaptive cruise control: a reinforcement learning approach. IEEE Trans. Intell. Transp. Syst. 12 (4), 1248–1260.
di Bernardo, M., Salvi, A., Santini, S., 2015. Distributed consensus strategy for platooning of vehicles in the presence of time varying heterogeneous communication delays. IEEE Trans. Intell. Transp. Syst. 16 (1), 102–112.
Feller, W., 1950. An Introduction to Probability Theory and its Applications, vol. 1. John Wiley & Sons, Inc.
Ge, J.I., Orosz, G., 2014. Dynamics of connected vehicle systems with delayed acceleration feedback. Transp. Res. Part C: Emerg. Technol. 46, 46–64.
Ge, J.I., Orosz, G., 2017. Optimal control of connected vehicle systems with communication delay and driver reaction time. IEEE Trans. Intell. Transp. Syst.
Ge, J.I., Orosz, G., Hajdu, D., Insperger, T., Moehlis, J., 2017. Time Delay Systems – Theory, Numerics, Applications, and Experiments, Advances in Delays and Dynamics, vol. 7. Springer, pp. 263–282. Ch. 18.
Henderson, H.V., Searle, S.R., 1981. On deriving the inverse of a sum of matrices. SIAM Rev. 23 (1), 53–60.
Ioannou, P.A., Chien, C.C., 1993. Autonomous intelligent cruise control. IEEE Trans. Veh. Technol. 42 (4), 657–672.
Jia, D., Ngoduy, D., 2016. Platoon based cooperative driving model with consideration of realistic inter-vehicle communication. Transp. Res. Part C: Emerg. Technol. 68, 245–264.
Kenney, J.B., 2011. Dedicated short-range communications (DSRC) standards in the United States. Proc. IEEE 99 (7), 1162–1182.
Laub, A., 2005. Matrix Analysis for Scientists and Engineers. The Society for Industrial and Applied Mathematics.
Li, S.E., Zheng, Y., Li, K., Wang, J., 2015. An overview of vehicular platoon control under the four-component framework. In: 2015 IEEE Intelligent Vehicles Symposium (IV), pp. 286–291.
Lidström, K., Sjöberg, K., Holmberg, U., Andersson, J., Bergh, F., Bjäde, M., Mak, S., 2012. A modular CACC system integration and design. IEEE Trans. Intell. Transp. Syst. 13 (3), 1050–1061.
Lioris, J., Pedarsani, R., Tascikaraoglu, F.Y., Varaiya, P., 2017. Platoons of connected vehicles can double throughput in urban roads. Transp. Res. Part C: Emerg. Technol. 77, 292–305.
Loan, C.F., 2000. The ubiquitous kronecker product. J. Comput. Appl. Math. 123 (1–2), 85–100.
Milanes, V., Alonso, J., Bouraoui, L., Ploeg, J., 2011. Cooperative maneuvering in close environments among cybercars and dual-mode cars. IEEE Trans. Intell. Transp. Syst. 12 (1), 15–24.
Milanes, V., Shladover, S., Spring, J., Nowakowski, C., Kawazoe, H., Nakamura, M., 2014. Cooperative adaptive cruise control in real traffic situations. IEEE Trans. Intell. Transp. Syst. 15 (1), 296–305.
Naus, G.J.L., Vugts, R.P.A., Ploeg, J., van de Molengraft, M.R.J.G., Steinbuch, M., 2010. String-stable CACC design and experimental validation: a frequency-domain approach. IEEE Trans. Veh. Technol. 59 (9), 429–436.
Nieuwenhuijze, M.R.I., van Keulen, T., Öncü, S., Bonsen, B., Nijmeijer, H., 2012. Cooperative driving with a heavy-duty truck in mixed traffic: experimental results. IEEE Trans. Intell. Transp. Syst. 13 (3), 1026–1032.
Olson, B.J., Shaw, S.W., Shi, C., Pierre, C., Parker, R.G., 2014. Circulant matrices and their application to vibration analysis. Appl. Mech. Rev. 66 (4).
Orosz, G., 2016. Connected cruise control: modeling, delay effects, and nonlinear behavior. Veh. Syst. Dyn. 54 (8), 1147–1176.
Orosz, G., Wilson, R.E., Stépán, G., 2010. Traffic jams: dynamics and control. Philos. Trans. Roy. Soc. A 368 (1928), 4455–4479.
Orosz, G., Wilson, R.E., Szalai, R., Stépán, G., 2009. Exciting traffic jams: nonlinear phenomena behind traffic jam formation on highways. Phys. Rev. E 80, 046205.
Ploeg, J., Semsar-Kazerooni, E., Lijster, G., van de Wouw, N., Nijmeijer, H., 2015. Graceful degradation of cooperative adaptive cruise control. IEEE Trans. Intell. Transp. Syst. 16 (1), 488–497.
Ploeg, J., Shladover, S., Nijmeier, H., de Wouw, N.V., 2012. Introduction to the special issue on the 2011 grand cooperative driving challenge. IEEE Trans. Intell. Transp. Syst. 13 (3), 989–993.
Ploeg, J., Shukla, D.P., van de Wouw, N., Nijmeijer, H., 2014a. Controller synthesis for string stability of vehicle platoons. IEEE Trans. Intell. Transp. Syst. 15 (2), 854–865.
Ploeg, J., van de Wouw, N., Nijmeijer, H., 2014b. Lp string stability of cascaded systems: application to vehicle platooning. IEEE Trans. Control Syst. Technol. 22 (2), 786–793.
Qin, W.B., Gomez, M.M., Orosz, G., 2017. Stability and frequency response under stochastic communication delays with applications to connected cruise control design. IEEE Trans. Intell. Transp. Syst. 18 (2), 388–403.
Qin, W.B., Orosz, G., 2013. Digital effects and delays in connected vehicles: linear stability and simulations. In: Proceedings of the ASME Dynamical Systems and Control Conference. No. DSCC2013-3830. ASME, pp. V002T30A001.
Rajamani, R., Shladover, S.E., 2001. An experimental comparative study of autonomous and cooperative vehicle-follower control systems. Transp. Res. Part C: Emerg. Technol. 9 (1), 15–31.
Rajamani, R., Zhu, C., 2002. Semi-autonomous adaptive cruise control systems. IEEE Trans. Veh. Technol. 51 (5), 1186–1192.
SAE J2735, 2016. Dedicated short range communications (DSRC) message set dictionary.
Schrank, D., Eisele, B., Lomax, T., Bak, J., 2015. 2015 urban mobility scorecard. Tech. rep., Texas A&M Transportation Institute.
Shladover, S.E., 1991. Longitudinal control of automotive vehicles in close-formation platoons. J. Dyn. Syst. Meas. Control 113 (2), 231–241.

Talebpour, A., Mahmassani, H.S., 2016. Influence of connected and autonomous vehicles on traffic flow stability and throughput. Transp. Res. Part C: Emerg. Technol. 71, 143–163.
Trefethen, L.N., Bau III, D., 1997. Numerical Linear Algebra. SIAM.
van Arem, B., van Driel, C.J.G., Visser, R., 2006. The impact of cooperative adaptive cruise control on traffic-flow characteristics. IEEE Trans. Intell. Transp. Syst. 7 (4), 429–436.
Wang, M., Daamen, W., Hoogendoorn, S.P., van Arem, B., 2014. Rolling horizon control framework for driver assistance systems. Part I: Mathematical formulation and non-cooperative systems. Transp. Res. Part C: Emerg. Technol. 40, 271–289.
Werf, J.V., Shladover, S.E., Miller, M.A., Kourjanskaia, N., 2002. Effects of adaptive cruise control systems on highway traffic flow capacity. Transp. Res. Rec.: J. Transp. Res. Board 1800 (1), 78–84.
Zhang, L., Orosz, G., 2016. Motif-based design for connected vehicle systems in presence of heterogeneous connectivity structures and time delays. IEEE Trans. Intell. Transp. Syst. 17 (6), 1638–1651.
Zhang, L., Orosz, G., 2017. Consensus and disturbance attenuation in multi-agent chains with nonlinear control and time delays. Int. J. Robust Nonlinear Control 27 (5), 781–803.
Zheng, Y., Li, S.E., Li, K., Wang, L.Y., 2016a. Stability margin improvement of vehicular platoon considering undirected topology and asymmetric control. IEEE Trans. Control Syst. Technol. 24 (4), 1253–1265.
Zheng, Y., Li, S.E., Wang, J., Cao, D., Li, K., 2016b. Stability and scalability of homogeneous vehicular platoon: study on the influence of information flow topologies. IEEE Trans. Intell. Transp. Syst. 17 (1), 14–26.